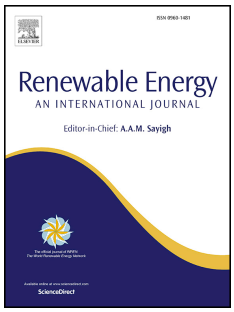

Wave resource characterization at regional and nearshore scales for the U.S. Alaska coast based on a 32-year high-resolution hindcast

Gabriel García-Medina, Zhaoqing Yang, Wei-Cheng Wu, Taiping Wang

PII: S0960-1481(21)00169-5

DOI: https://doi.org/10.1016/j.renene.2021.02.005

Reference: RENE 14895

To appear in: *Renewable Energy*

Received Date: 12 November 2020

Revised Date: 30 January 2021

Accepted Date: 1 February 2021

Please cite this article as: García-Medina G, Yang Z, Wu W-C, Wang T, Wave resource characterization at regional and nearshore scales for the U.S. Alaska coast based on a 32-year high-resolution hindcast, *Renewable Energy*, https://doi.org/10.1016/j.renene.2021.02.005.

Submitted to Renewable Energy: RENE-D-20-05820R1

Wave resource characterization at regional and nearshore scales for the U.S. Alaska coast based on a 32-year high-resolution hindcast

Gabriel García-Medina[1], Zhaoqing Yang[1,2,*], Wei-Cheng Wu[1,3], and Taiping Wang[1]

[1]Coastal Sciences Division, Pacific Northwest National Laboratory, Seattle, WA, USA

[2]University of Washington, Department of Civil and Environmental Engineering. Seattle, WA, USA

[3]Present Address: DSI, LLC, Edmonds, WA, USA

* Corresponding author: zhaoqing.yang@pnnl.gov

Abstract

A wave resource characterization was performed for the southern coast of Alaska based on a 32-year hindcast covering the period from 1979 to 2010. The characterization closely followed International Electrotechnical Commission (IEC) Technical Specifications. An unstructured-grid Simulating WAves Nearshore (SWAN) model, which had an approximate spatial resolution of 300 m within 30 km from the nearest shoreline, was developed. Extensive model validation and error characterization was performed. The model was found to perform well with an average absolute percent error of 8.6% in significant wave height, averaged over 18 buoys. Statistics for the six IEC wave resource parameters were calculated and aggregated at 20 km from shore to quantify the incident wave power and its variability at a regional scale. The southern coast of the Aleutian Archipelago was found to have the most available wave energy in the region. A nearshore resource assessment was performed by evaluating resource hotspots located 1 km from shore. More than 28% of the nearshore stations analyzed had an Optimum

Hotspot Identifier value of at least 5 [kW/m] at diverse water depths, thereby positioning Alaska as a promising location for wave energy development.

Submitted to Renewable Energy: RENE-D-20-05820R1

Wave resource characterization at regional and nearshore scales for the U.S. Alaska coast based on a 32-year high-resolution hindcast

Gabriel García-Medina[1], Zhaoqing Yang[1,2,*], Wei-Cheng Wu[1,3], and Taiping Wang[1]

[1]Coastal Sciences Division, Pacific Northwest National Laboratory, Seattle, WA, USA

[2]University of Washington, Department of Civil and Environmental Engineering. Seattle, WA, USA

[3]Present Address: DSI, LLC, Edmonds, WA, USA

* Corresponding author: zhaoqing.yang@pnnl.gov

Abstract

A wave resource characterization was performed for the southern coast of Alaska based on a 32-year hindcast covering the period from 1979 to 2010. The characterization closely followed International Electrotechnical Commission (IEC) Technical Specifications. An unstructured-grid Simulating WAves Nearshore (SWAN) model, which had an approximate spatial resolution of 300 m within 30 km from the nearest shoreline, was developed. Extensive model validation and error characterization was performed. The model was found to perform well with an average absolute percent error of 8.6% in significant wave height, averaged over 18 buoys. Statistics for the six IEC wave resource parameters were calculated and aggregated at 20 km from shore to quantify the incident wave power and its variability at a regional scale. The southern coast of the Aleutian Archipelago was found to have the most available wave energy in the region. A nearshore resource assessment was performed by evaluating resource hotspots located 1 km from shore. More than 28% of the nearshore stations analyzed had an Optimum

Hotspot Identifier value of at least 5 [kW/m] at diverse water depths, thereby positioning Alaska as a promising location for wave energy development.

Key words: wave energy resource, wave climate, Alaska Coast, SWAN, WW3, hot spots

Highlights:

- A high-resolution wave model covering the southern Alaska coast was developed and validated.
- The first systemic wave resource characterization of southern Alaska following IEC-TS 62600-101
- The southern coast of the Aleutian Archipelago has the highest annual wave power at 45.4 kW/m
- Southeast Alaska and the Aleutian Archipelago had the most nearshore hotspots with Optimum Hotspot Identifier > 5 kW/m

1 Introduction

Interest in harvesting marine renewable energy has increased in recent decades as the world works toward decarbonizing energy production. Global wave energy is a vast resource whose theoretical value has been estimated to be over 2 TW [1]. Global wave resource assessments have identified the North Pacific Ocean as an energetic region with offshore wave power density in excess of 35 kW/m in the winter [2,3], with the coast of Alaska being identified as a high energy ocean coast [4]. Exploitation of this resource could help offset carbon emissions and develop new offshore markets. Wave resource characterization is a crucial first step in the planning, design, and development of wave-powered energy generation [5]. The wave energy resource of the United States (U.S.) has been characterized in detail at a national (large) scale [6,7] and regionally for the East Coast [8,9], West Coast [10–16], Caribbean [17], and Hawaii [18–20]. While most of the coastal waters of the U.S. have been characterized, to the authors' knowledge no nearshore wave energy resource based on long-term wave hindcasts has been performed for the Alaska coastal region.

Global assessments serve to identify energetic offshore regions and these studies employ numerical wave models because long term in situ measurements are not widely available. Barstow et al. [21] produced an early global wave resource characterization based on two years of data derived from satellite borne altimeters that required estimating the wave period but gave a first order estimate of the resource. Follow up studies circumvented the limitations of this study using model hindcasts. Cornett [3] evaluated the global wave resource using a 10-year hindcast at with a resolution of 1.25° by 1.0° (139 km by 111 km at the Equator). The wave power was estimated from significant wave height and the peak period assuming deep water conditions. Arinaga and Cheung [2] evaluated the global wave power using a 10-year hindcast with the same

spatial resolution but focused on the different components of the sea state, which adds directional wave information indirectly as the sea state characterization comes from a partitioned, directionally resolved wave spectrum. The wave resource was characterized based on significant wave height, mean period, and wave power. In parallel to these developments, Electric Power Research Institute (EPRI) performed a large scale wave resource assessment for the U.S. based on buoy data [22] which was then superseded with a 51 month hindcast at a 4 arc-minute resolution [6]. This assessment identified the waters off the Alaskan coast as the most energetic in the U.S. and presented integrated wave power for the inner shelf based on a reconstruction of the wave spectrum from partitioned parameters. Historically, the directional characteristics of the resource have not been studied at a large scale. However, recently, Ahn et al [7] evaluated the main partitions and classified the wave climate along the U.S. coastal waters and included the general directionality of the resource. That study used results from a 30-year hindcast at a 4 arc-minute resolution. All these studies point to Alaska as a promising location for wave energy harvesting. This warrants a detailed assessment that considers the complete directionality of the resource, an accurate representation of shallow water effects, and a long-term dataset. Furthermore, the analysis of the results and the parameters evaluated differ from study to study making it difficult to compare between them. This can be addressed by performing an assessment following industry standard methodology. If wave power and other wave resource characterization parameters are directly computed from the model output, no approximations (e.g. via spectral reconstruction) will be necessary.

Alaska, through House Bill No. 306 adopted in 2010, has set a goal to generate 50% of its electricity from renewable sources by 2025. The respective costs of electricity for residential, commercial, and industrial sectors are 73%, 80%, and 148% higher than the U.S. average as of

September 2020 (https://www.eia.gov/state/?sid=AK accessed 5 January 2021). The electric grid in Alaska is not connected to major grids such as the Western Interconnection, making it an energetically vulnerable region. This vulnerability is further exacerbated in the Alaskan islands, where, for instance, the Aleutian Islands are not connected to any of the larger regional grids in mainland Alaska. Many of the rural communities rely on expensive diesel electric generators for power (https://www.eia.gov/state/?sid=AK accessed 5 January 2021). The combination of high prices and the vulnerability of the grid make Alaska a compelling place to develop renewable energy production, including wave energy. While several wave energy converters (WECs) have been tested around the world, no WEC has been tested in Alaska. One of the reasons for this is the lack of detailed wave information for developers and stakeholders.

The most promising area for WEC developments lies on the nearshore, in part because of the associated electricity transmission and maintenance capabilities [23]. Waves in the nearshore are affected by bathymetry mainly through refraction and depth-induced breaking. Because long-term and spatially dense monitoring of waves is not available in Alaska, a numerical study of the wave resource is necessary. State-of-the-art numerical models have the capacity for simulating the wave climate, including the effects of nearshore and shallow water physics, with great accuracy [24]. This paper presents a detailed modeling study of wave resource characterization focused on nearshore (within 20 km from shore) Alaska to address the knowledge gaps in the region. A 32-year hindcast (1979–2010) covering the southern portion of the Exclusive Economic Zone (EEZ, 200 nautical miles from shore) around southern Alaska was performed. The model developed as part of this study closely follows the recommendations of the International Electrotechnical Commission Technical Specification (IEC-TS) 62600-101 for marine energy [25] for a Class 2 (feasibility) wave resource characterization. The present model

has a spatial resolution of ~300 m in the 30 km adjacent to the main coastlines and islands, which complies with the IEC-TS requirements of 500 m spatial resolution. Note that the IEC-TS specifies the resolution for a computational grid composed of quadrilateral elements. This is equivalent to a side length of 760 m for computational grids composed of triangular elements which is the type of grid used in this study. The IEC-TS also specifies the physical processes that need to be accounted for and the types of models used, further information about the compliance of this study with the IEC-TS is presented in Section 2.2.

Using the model results, the nearshore resource is assessed following the IEC-TS guidelines for reporting and analysis. In addition, the monthly, seasonal, and yearly variability indices, and the Optimum Hotspot Identifier (OHI) values were computed to evaluate the wave resource. These are device agnostic parameters that characterize the suitability of a location for energy exploitation based on the temporal variability of the resource.

The rest of the paper is structured as follows: the methodology and model description are provided in Section 2. The model validation and error characterization are presented in Section 3. The regional wave resource characterization based on IEC-TS is presented in Section 4. Section 5 assesses the nearshore resource at virtual stations located 1 km from shore. Finally, the conclusions of the study are presented in Section **Error! Reference source not found.**.

2 Methods

2.1 Study area

There are two main reasons that Alaska has the largest wave energy resource in the U.S. [6]. First, it has the longest coastline of any U.S. state, thus when aggregating the results Electric Power Research Institute (EPRI, [6]) found Alaska had the largest potential of all regions.

Second, the southern coast is exposed to the energetic Pacific Ocean swells and strong locally generated waves [e.g. 2]. The waves in the northern Pacific Ocean are characterized by energetic winters and calmer summers [e.g. 2].

Alaska borders multiple basins in the Pacific and Arctic Oceans, including the Gulf of Alaska, the Aleutian Basin, Bering Sea, Beaufort Sea, and Chukchi Sea (see Fig. 1). Because of its large area, great diversity in the wave climate is expected regionally in Alaska. Sea ice has been historically present along the Arctic and Bering coasts of Alaska during the winter and spring, but the conditions in the Arctic Ocean and the northern Bering Sea are changing rapidly [26–28]. At the current rate of change in sea ice coverage, the wave climate for the first decade of this century might not be representative of the conditions at the time of this writing. Therefore, we decided not to include the Arctic and North Bearing Sea in the 32-year analysis. Based on Climate Forecast System Reanalysis (CFSR, [29]) data, Bristol Bay was ice free, 95% of the time (Fig. 1a) during the hindcast period. There have been times, however, when large portions of Bristol Bay were ice covered. We decided to include Bristol Bay as part of the model because it is mostly ice free. However, it must be acknowledged that the historical wave climatology will be overestimated in its intensity during winter and early spring in this region because the Simulating WAves Nearshore (SWAN) model version used in this study does not consider the effect of sea ice. In addition, we excluded Cook Inlet from the analysis because of the known presence of sea ice during the winter and spring [30] even though the inlet is included in the model domain.

The study area thus extends westward from Cape Newenham at the north end of Bristol Bay until it meets the EEZ line, and follows the line around the Aleutian Islands to the

149 southeastern part of the state at the Dixon Entrance where it reaches the U.S.-Canada border
150 (Fig. 1). This domain covers 2,836,000 km^2 of the 3,770,000 km^2 of the U.S EEZ around Alaska.

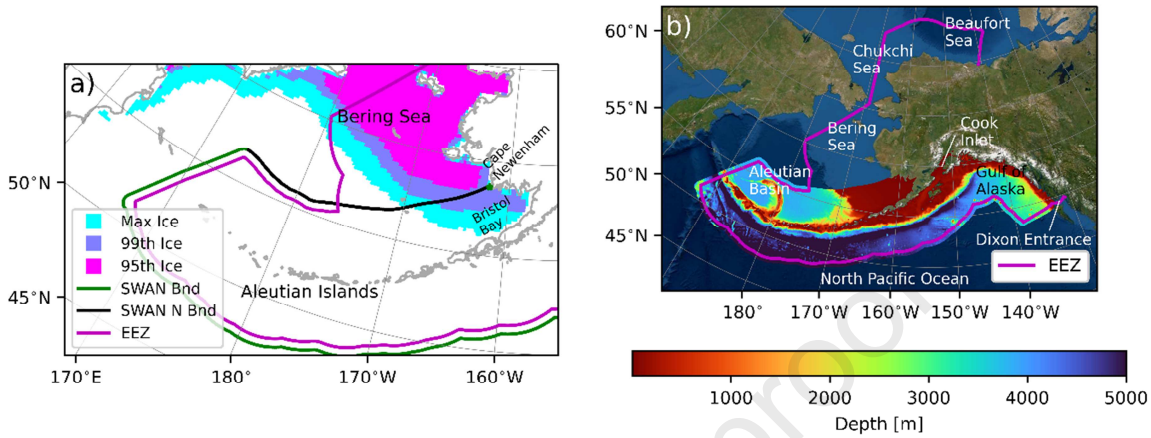

151

152 Fig. 1. (a) Maximum, 99th percentile, and 95th percentile sea ice extent from 1979 to 2010 in
153 Western Alaska. SWAN Bnd is the open boundary condition of the model and SWAN N Bnd
154 is the northern section of the open boundary. (b) Bathymetry for the wave model with the
155 U.S. Exclusive Economic Zone overlaid.

156 **2.2 Regional wave models**

157 The primary model used for simulating and characterizing the nearshore wave climate of
158 Alaska is SWAN Cycle III Version 41.10 [31,32]. SWAN is a third-generation model that solves
159 the spectral action balance equation:

$$\frac{\partial N}{\partial t} + \frac{\partial c_x N}{\partial x} + \frac{\partial c_y N}{\partial y} + \frac{\partial c_\theta N}{\partial \theta} + \frac{\partial c_\sigma N}{\partial \sigma} = \frac{1}{\sigma}(S_{in} + S_{wc} + S_{nl4} + S_{bot} + S_{brk}) \quad (1)$$

160 where N is the wave action, c_x and c_y are the group velocity in the spatial dimensions, c_θ and c_σ
161 are the propagation velocities in spectral space, θ is the wave direction, and σ is the radian
162 frequency of the waves. The right-hand side represents the sinks and sources of energy. Wind
163 input (S_{in}) and whitecapping (S_{wc}) were simulated with the SWAN default formulations using
164 the Komen et al. [33] method. As part of the wind input source term, initial linear growth was
165 activated using the Cavaleri Malanotte-Rizzoli [34] method. Non-linear quadruplet interactions

(S_{nl}) were simulated using the Discrete Interaction Approximation [35]. Finally, dissipation due to bottom friction (S_{bot}) and depth-induced wave breaking (S_{brk}) were modeled based on the JONSWAP [36] and Battjes and Janssen [37] formulations, respectively. Energy transfers due to triad interaction were not included in the model. All source terms used the default coefficients in SWAN 41.10. The effects of water levels and currents have not been considered in the hindcast, which could be important in areas of high speed currents (see Guillou et al. [38] and references therein), such as Cook Inlet and the Inside Passage (not included in this model). However, because the ocean currents are weak over most of the domain [39] these are not expected to significantly affect the waves [40]. The inclusion varying water levels and currents are recommended for localized Class 3 resource assessments in areas where currents and tides affect the waves. In this study we used the unstructured mesh implementation of SWAN, which uses an implicit, unconditionally stable, finite difference solution scheme [41]. Implicit solutions are more computationally efficient for large models at high spatial resolutions than explicit models (see Cavaleri et al. [24] and references therein). In addition, SWAN was selected as the basis for the numerical model because it has been implemented successfully in many other regions for similar recent wave resource assessments [17,18,42–55]; with many of these studies implementing the unstructured mesh version of SWAN [13,42,43,46,48,50,51,54,55].

This model was configured to be homologated as a Class 2 (feasibility) resource assessment in accordance with IEC-TS 62600-101 [25]. Table 1 shows the IEC-TS homologation for the most important parameters. The model mesh was configured with a resolution of 300 m or higher in the region between the coastline and 30 km from shore (Fig. 2a). This ensured that the area where WECs are more likely to be installed was resolved at a resolution that allows for feasibility (Class 2) studies [23]. Thirty kilometers from shore the resolution was relaxed until it

reached a 4 km resolution at the open boundary. This resulted in a computational domain with 3,894,283 nodes and 7,719,870 elements. Fig. 2b-c shows the model mesh around the Andreanof Islands and Fox Islands in the Aleutian Archipelago. The model bathymetry comes from the Southern Alaska Coastal Relief Model [56], and National Oceanic and Atmospheric Administration (NOAA) Fisheries digital elevation models [57–59].

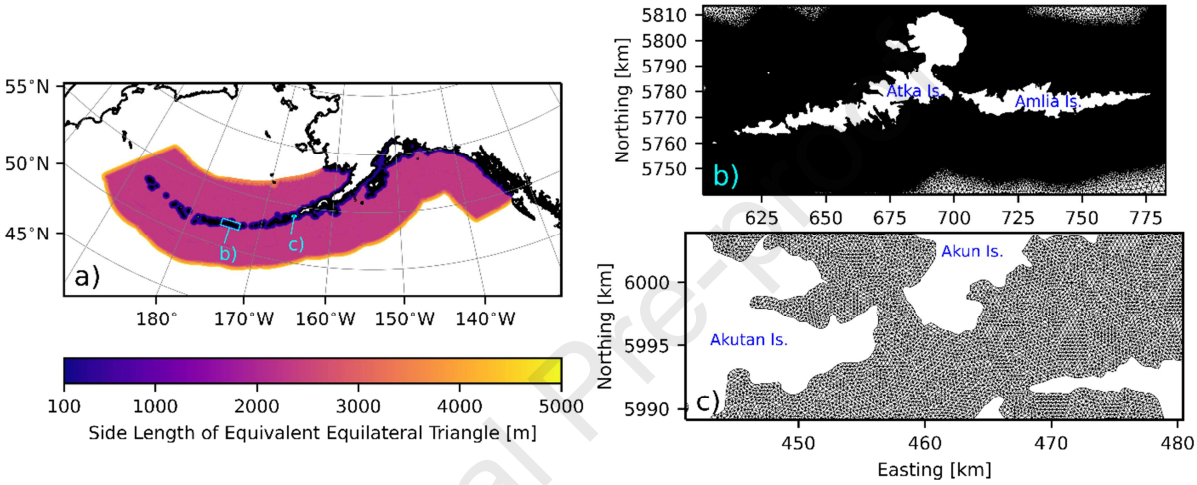

Fig. 2. (a) Model mesh resolution. Mesh examples around the (b) Andreanof Islands and (c) eastern Fox Islands. Locations of panels b and c are outlined in turquoise in panel a.

The spectral grid was discretized with 29 logarithmically spaced frequencies from 0.035 to 0.505 Hz. The spectral resolution was increased from the IEC-TS–recommended 10° to 5° to alleviate the Garden Sprinkler Effect, which was assessed qualitatively and discussed in a study report [60]. The model was solved in non-stationary mode with a 10-minute time step. A maximum of two iterations per integration time step were allowed in order to maximize computational efficiency. This number of iterations was determined via convergence analysis (not shown), and the results were consistent with a similar study of the U.S. East Coast [43], where it was found that limiting the number of iterations did not adversely affect model performance.

Table 1. IEC-TS Class 2 model homologation. Recommended values are *italicized*.

Parameter	IEC-TS Requirement	This Study
Wind temporal resolution	3 h	1 h
Wind spatial resolution	50 km	Zonal: 32 km at 55° Meridional: 55 km
Spectral boundary conditions	Yes	Yes
Third-generation physics	Yes	Yes
Shallow water physics	Yes	Yes
Sea ice	Yes	Considered in WW3
Water-level variations	Yes	No[a]
Wave-current interactions	Yes	No[a]
Minimum spatial resolution	500 m	300 m
Minimum number of frequencies	25	29
Frequency range	0.04 – 0.5 Hz	0.035 – 0.505 Hz
Directional resolution	10°	5°

[a]This could be important in the Inside Passage, Cook Inlet, and Prince William Sound. These areas were not analyzed for wave energy resource in this study.
WW3 = Wavewatch III®

Spectral boundary conditions are provided at an hourly resolution at every boundary node, each of which are specified at 4 km intervals, by a reimplementation the Wavewatch III® (WW3) multi-grid model run operationally by NOAA National Centers for Environmental Prediction [61]. This system consists of three levels of nesting ranging from a 0.5 arc-degree resolution model with global coverage to an 8 by 4 arc-minute model providing coverage closer to shore (see Table 2). The modeling system extends northward from the Bering Strait into the Arctic Ocean, thereby providing complete coverage of the Bering Sea. The inclusion of this region was important for providing boundary conditions to the northern end of the regional model (discussed in Section 2.1). This multi-level method for providing open boundary conditions has been used extensively in previous wave resource characterization studies [e.g. 11–14,17,49].

WW3 is also a third-generation spectral wave model that solves the action balance equation. However, WW3 solves that equation using a different numerical method and employs different parameterizations for some source terms in comparison to SWAN. In this study we

used the ST4 physics package option in WW3 to simulate S_{in} and S_{ds} [62]. The non-linear quadruplet interactions, bottom friction, and depth-induced breaking were modeled with the same formulations used in SWAN. Default parameters were used for all free parameters in the source term equations. Sea ice was implemented using the subgrid obstruction model based on ice concentration [63]. The effects of scattering and wave damping were not included in the model. Ice concentration cutoffs of 0.25 and 0.75 were used to define the level of wave energy obstruction at each grid cell following the Tolman [63] method. Thus, partial wave energy blockage occurs at model cells with ice concentration values in this range.

The WW3 simulations used 29 frequency bins, 24 direction bins, and a frequency range from 0.035 Hz to 0.505 Hz with bins increasing logarithmically by a factor of 1.1. WW3 has an explicit solution scheme that requires four time steps per model: the global time step (Δt_g), the spatial propagation time step (Δt_{xy}), the intra-spectral propagation time step (Δt_k), and the source term integration time step (Δt_s). The time steps used in the model are summarized in Table 2.

Table 2. Wavewatch III model parameters.

Model Name	Coverage	Resolution (lon x lat)	Time Steps (s)			
			Δt_g	Δt_{xy}	Δt_k	Δts
Global (L1)	77.5°S – 77.5°N; 0 – 360°W	0.5° × 0.5°	1800	600	900	30
Alaska 10 m (L2)	44° – 75°N; 140°E – 120°W	15' × 10'	1800	225	900	15
Alaska 4 m (L3)	48° – 74°N; 165°E – 122°W	8' × 4'	600	150	300	15

2.3 Surface and open boundary forcing

Wind forcing for the wave model comes from the CFSR [29]. This forcing was chosen for its consistency with other resource assessments in the U.S. [12–14,43]. CFSR covers the 32-year period from 1979 to 2010 with a consistent model configuration. The analysis period exceeds the 10-year period recommended by the IEC-TS. Seasonally averaged wind magnitude and direction

241 over the study period are shown in Fig. 3. Wind speed over the study area varies seasonally, with
242 stronger winds in the winter and weaker winds in the summer. The wind direction is also
243 variable over the domain. During the summer, winds blow poleward in the southern Bering Sea
244 and the direction reverses during the winter and the shoulder seasons. Throughout the year the
245 wind blows northward in the Gulf of Alaska. These wind patterns have an effect on the locally
246 generated waves, thus affecting the distribution and magnitude of energy at high frequencies
247 (i.e., small wave periods). For a detailed assessment of wind offshore of Alaska, refer to
248 Doubrawa Moreira et al. [64].

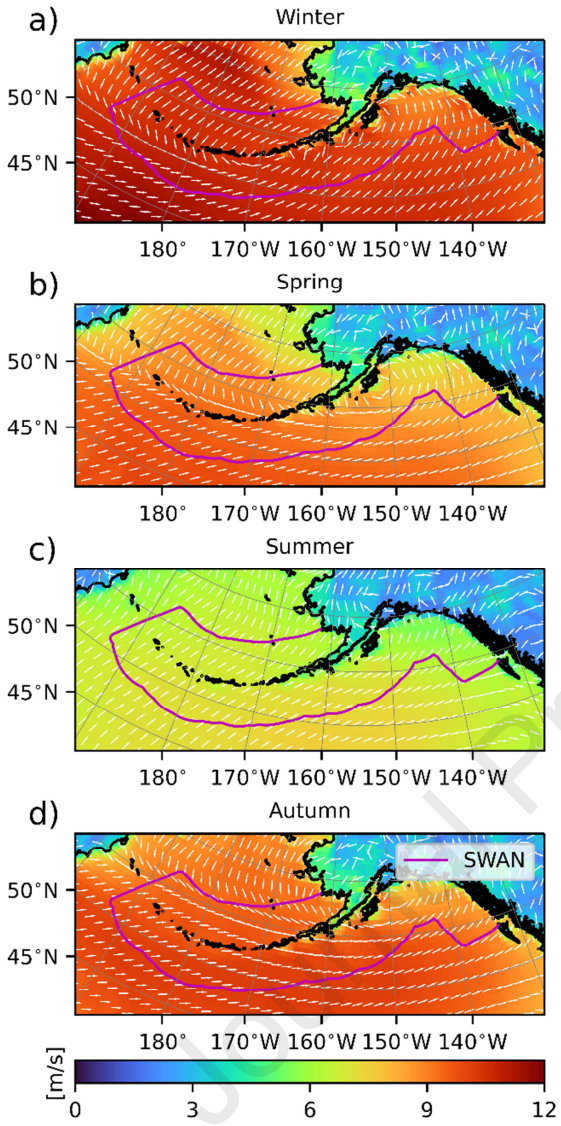

Fig. 3. Seasonal wind speed and direction 10 m above the surface near Alaska. (a) Winter: December, January, and February; (b) Spring: March, April, and May; (c) Summer: June, July, and August; and (d) Autumn: September, October, and November.

The study area was delimited by the EEZ and the presence of sea ice. However, the effect of the sea ice on the waves in the Bering Sea must be captured at the boundaries. Sea ice concentration is included in the WW3 model at a 0.5° resolution obtained from CFSR at daily intervals; this data set has been used by other large-scale models [61]. Fig. 4 shows the monthly averaged significant wave height at the northern boundary of the SWAN model (shown in Fig. 1a as SWAN N Bnd). During the boreal summer, waves do not show a strong decline in height

east of 170°W. During the winter and spring, sharp declines in significant wave height (H_{m0}) are seen in that region. That sharp decrease in H_{m0} is attributed to the presence of sea ice in the northern Bering Sea. Its effect on waves is captured by all levels of WW3 and reflected in the open boundary forcing of the SWAN model.

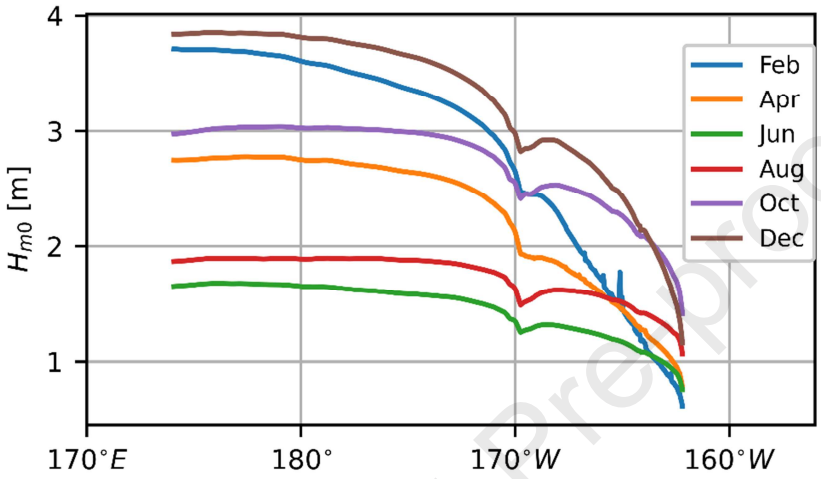

Fig. 4. Average significant wave height during the hindcast period (1979–2010) for selected months at the northern boundary of SWAN (see Fig. 1a for location).

2.4 Representation of the wave energy resource

Integrated wave parameters represent the complete sea state and provide the means to characterize the wave climate for wave energy purposes. Following IEC-TS, the energy transport, energy content, period, and directionality of the waves can be represented by six parameters. The omnidirectional wave power $(J\ [W/m])$ describes the flux of energy through a unit circle and describes the density of power:

$$J = \rho g \sum_{i,j} c_{g,i} S_{ij} \Delta f_i \Delta \theta_j \qquad (2)$$

where ρ is the water density, g is the acceleration of gravity, c_g is the group velocity defined based on linear wave theory, S_{ij} is the directionally and frequency resolved variance spectrum with units of $\frac{m^2}{Hz-deg}$, f is the discrete frequency, and θ is the discrete wave direction.

The significant wave height provides a characteristic wave height of the sea state and is defined as:

$$H_{m0} = 4.004\sqrt{m_0} \tag{3}$$

where m_0 is the zeroth spectral moment. Spectral moments are computed from the variance spectrum via:

$$m_n = \sum_i f_i^n \left(\sum_j S_{ij} \Delta\theta_j \right) \Delta f_i \tag{4}$$

Following linear wave theory, $H_{m0}\ [m]$ is directly proportional to the total energy of the sea state:

$$E = \frac{1}{16} \rho g (H_{m0})^2. \tag{5}$$

The energy period ($T_e\ [s]$) is presented as a characteristic wave period:

$$T_e = \frac{m_{-1}}{m_0} \tag{6}$$

where the spectral moments are computed following equation (4). The spectral width (ϵ_0) characterizes the spread of the energy in frequency space:

$$\epsilon_0 = \sqrt{\frac{m_{-0} m_{-2}}{m_{-1}^2} - 1} \tag{7}$$

Monochromatic sea states, where all waves have the same period, have an ϵ_0 of zero, this parameter is non-dimensional. Up to this point all parameters introduced have been agnostic of

wave directionality. The directional characteristics of the sea state can be described by the directionally resolved wave power:

$$J_\theta = \rho g \sum_{i,j} c_{g,i} S_{ij} \Delta f_i \Delta\theta_j \cos(\theta - \theta_j)\delta \qquad \begin{cases} \delta = 1, \cos(\theta - \theta_j) \geq 0 \\ \delta = 0, \cos(\theta - \theta_j) < 0 \end{cases} \tag{8}$$

where only the wave power crossing a vertical plane perpendicular to a direction θ is accounted for. The direction of maximum directionally resolved wave power θ_{Jmax} is the direction that maximizes J_θ. The directionality coefficient (d) characterizes the directional spread of wave power:

$$d = \frac{J_{\theta_{Jmax}}}{J} \tag{9}$$

where $J_{\theta_{Jmax}}[W/m]$ is the wave power at θ_{Jmax}. These parameters provide a comprehensive description of the sea state adequate for a reconnaissance study.

2.5 Assessment parameters

Several parameters are defined to assess the suitability of a location for wave energy harvesting. The Monthly Variability Index (MVI), Seasonal Variability Index (SVI), and Annual Variability Index (AVI) are device-agnostic indices that describe the temporal variability of the resource variability [3,65,66]. These parameters are defined as follows:

$$MVI = \frac{\bar{J}_{m,max} - \bar{J}_{m,min}}{\bar{J}} \tag{10}$$

$$SVI = \frac{\bar{J}_{s,max} - \bar{J}_{s,min}}{\bar{J}} \tag{11}$$

$$AVI = \frac{\bar{J}_{y,max} - \bar{J}_{y,min}}{\bar{J}} \tag{12}$$

where $\bar{J}_m$, $\bar{J}_s$, and $\bar{J}_y$ represent a monthly average, seasonal average, and yearly average, respectively. $\bar{J}$ represents the long-term average wave power.

In this study we did not assess the resource for a particular technology or device because at these early stages of development the power takeoff details are expected to change. The OHI [67] is an indicator for assessing the suitability of a location for energy extraction that is technology agnostic:

$$OHI = \frac{\bar{J}\, F(J > 2kW/m)}{MVI} \tag{13}$$

where $F(J > 2kW/m)$ is the fraction of time the sea state exceeds 2 kW/m. A higher OHI value represents a more desirable location for wave energy harvesting. This parameter favors locations that have large and consistent power and low monthly variability. The OHI has been computed for hotspot identification in other regions (e.g., Persian Gulf [67], India [68], China [50]).

3 Model validation

To ensure the validity of the hindcast, we perform extensive model-data comparisons and error characterizations using the IEC-TS-recommended methodology. First, the normalized errors (e) for each parameter (p), normalized for all variables except θ_{Jmax}, are computed as follows:

$$\mathrm{e}_p = \left[\frac{P_i - M_i}{M_i}\right] \tag{14}$$

where M_i are the measured data and P_i are the predicted results. When the observations and model results do not align in time, the latter are interpolated in time to match the former. The frequency resolution of the measured spectra is not constant over time and between buoys. For a

consistent comparison, all integrated parameters are computed from 0.035 to 0.4 Hz because this range is covered by both the model and data.

The quantitative metrics for model-data comparison are the mean systematic error $b(e_p)$ and mean random errors $re(e_p)$, which are expressed as percentages (except for θ_{Jmax}, which is expressed as degrees) and computed as follows:

$$\mathrm{b}(e_p) = 100 \sum_{SS} w\mu = 100 \sum_{SS} w \frac{1}{N} \sum_{i=1}^{N} e_p \tag{15}$$

$$re(e_p) = 100 \sum_{SS} w \sqrt{\frac{1}{N-1} \sum_{i=1}^{N} (e_p - \mu)^2} \tag{16}$$

where SS represents summation of the sea-state matrix, N is the number of observations, w is the weight, and μ is the mean value of parameter p. The errors are weighted based on the frequency of occurrence of the associated sea state and the mean wave power. The weights are specified by computing the probability density function of a sea state (SS) based on H_{m0} and T_e, where the data are binned, and the mean power of each bin is computed. In this study, H_{m0} and T_e were discretized every 0.5 m and 1 s, respectively. The weights are defined as the product of the mean power in each bin and the frequency of occurrence of each H_{m0} and T_e pairs. The resulting weight matrix is normalized such that the sum is unity. Finally, only SS bins that have more than five observations were considered for the statistical analysis.

Many studies perform model-data comparisons using a set of statistics different from those recommended by the IEC-TS [2,11,12,14,17,18,43,69] such as root-mean-square-error, scatter index, and linear correlation coefficient. Appendix A presents the model-data comparison using these statistics to allow for direct comparison between this study and others.

3.1 Buoy data for model validation

Eighteen buoys were deployed within the SWAN domain during the hindcast period, all of them owned and maintained by the National Data Buoy Center (NDBC). The buoy network provides coverage of the model domain (Fig. 5). Station 46003 (not shown) was not considered because of its proximity to Station 46066. Frequency-dependent data are available for a significant part of the hindcast period (Table 3). The availability of directional data is limited to three buoys during the hindcast period, and one of them provided less than four months of coverage.

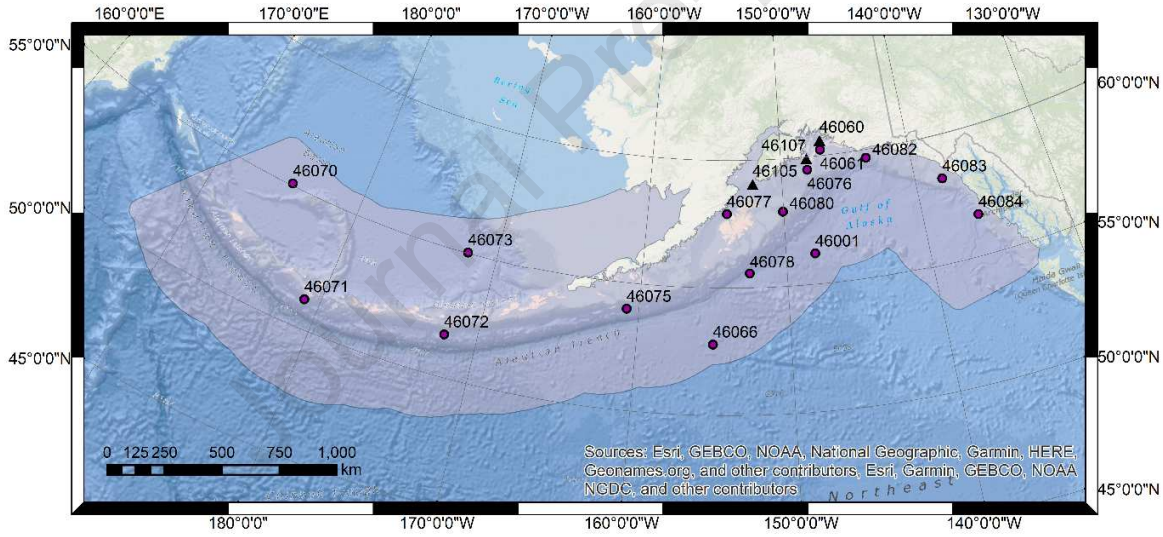

Fig. 5. Location of the NDBC wave buoys used for model validation and the SWAN domain (shaded). Triangles represent stations for which directional data are available. Circles represent stations for which only bulk parameters are available.

Table 3. Summary of wave buoys for model validation. All stations are owned and maintained by NDBC. Ranges are provided if the measurements have been discontinued. Gray-colored font indicates the data do not overlap with the hindcast period.

Buoy ID	Longitude	Latitude	Depth	Bulk Parameters	Frequency Spectrum	Directional Spectrum

			(m)	Availability since		
46001	-147.949	56.232	4054	1979	1996	2017
46060	-146.806	60.584	440	1995	1996	2007
46061	-146.843	60.230	220	1995	1996	2014
46066	-155.047	52.785	4545	2000	2000	2013
46070	175.153	55.082	3835	2006	2006	2015
46071	179.012	51.125	1681	2004	2004	2016
46072	-172.058	51.656	3048	2002	2002	2016
46073	-172.001	55.031	3052	2005	2005	2014
46075	-160.817	53.983	2393	2004	2004	2016
46076	-147.990	59.502	195	2005	2005	2015
46077	-154.175	57.910	202	2005	2005	2017
46078	-152.582	55.556	5380	2004	2004	2013
46080	-150.042	57.947	255	2002	2002	2017
46082	-143.372	59.681	300	2002	2002	2015
46083	-137.997	58.300	136	2001	2001	2015
46084	-136.101	56.600	1408	2002	2002	2016
46105[a]	-152.233	59.049	127	2008 – 2012	2008 – 2012	2008 – 2012
46107	-147.992	59.925	106	2008 – 2010	2008 – 2010	2008 – 2010

[a] Buoy 46105 was only active between 3 August 2008 and 26 December 2008 during the hindcast period.

353

354 **3.2 Model-data comparison**

355 Model-data comparisons conducted in accordance with the IEC-TS recommendations are
356 summarized in Table 4. The model errors fall within the IEC-TS Class 1 limits in most cases. At
357 most stations, the Class 2 limits are satisfied for the mean error in H_{m0}. One notable exception in
358 meeting the error requirements by the IEC-TS is the random error in omnidirectional wave
359 power, where Class 1 limits are met in only one station (46070). It is important to mention that
360 traditional error statistics (see Appendix A) suggest model performance is comparable to or
361 exceeds the performance of similar modeling studies [e.g. 2]. This suggests that the IEC-TS
362 requirements are very strict. In general, poor model performance is observed at the mouth of
363 Cook Inlet (46105), Shelikof Strait (46077), and Prince William Sound (46060, 46061). These

364 errors can be attributed, in part, to the wind forcing performance in these semi-enclosed areas
365 (see Appendix A). Results in these areas are presented in the rest of this manuscript but the
366 reader is urged to interpret the results with the model performance errors in mind. The model
367 performance errors in these areas indicate the need for improvements in future higher-class
368 localized resource assessments. Model performance in narrow seas and semi-enclosed basins has
369 been shown to improve with the inclusion of high-resolution wind fields [e.g. 70,71].

370 Table 4. Model validation for IEC-TS parameters. **Bold** text identifies buoys that meet the
371 criteria for a Class 1 assessment and are ***italicized*** if they meet the requirements for a Class 2
372 assessment. The mean systematic error (b) and mean random errors (re) are defined in
373 Section 3.1.

	H_{m0}		J		T_e		ϵ_0		θ_{Jmax}		d	
Buoy	b	re	b	re	b	re	b	re	B	re	b	re
Class 1 Maximum	10	15	25	35	10	15	-	-	-	-	-	-
Class 2 Maximum	5	10	12	25	5	10	12	25	10°	15°	12	25
46001	***2.6***	**14.8**	**17.9**	42.5	**7.6**	***8.8***	***-1.9***	***11.7***	-	-	-	-
46060	16.0	33.2	82.7	120.5	23.2	24.6	***-4.8***	26.8	12.3°	40.7°	43.7	19.6
46061	14.0	22.0	47.8	66.9	**7.7**	**10.9**	***-9.7***	13.1	-	-	-	-
46066	***2.8***	17.9	**21.3**	97.1	**8.1**	***9.3***	***-0.6***	***11.9***	-	-	-	-
46070	***-2.8***	**11.4**	***5.6***	**31.2**	**8.2**	***7.1***	***-0.1***	***10.3***	-	-	-	-
46071	***2.6***	15.9	**18.5**	48.2	**7.5**	***7.9***	***2.7***	***11.4***	-	-	-	-
46072	***1.7***	17.1	**15.6**	62.4	**6.0**	***8.9***	***-1.2***	***12.2***	-	-	-	-
46073	**5.3**	**14.5**	**20.7**	46.7	***4.8***	***6.7***	***7.6***	***11.0***	-	-	-	-
46075	***3.0***	15.4	**16.8**	42.4	**5.5**	***8.2***	***-0.9***	***11.7***	-	-	-	-
46076	***3.4***	16.3	25.1	51.3	**10.6**	***10.0***	***5.2***	***14.2***	-	-	-	-
46077	-15.9	25.6	***-4.2***	79.3	15.1	20.1	32.3	42.1	-	-	-	-
46078	***2.0***	15.9	**14.6**	44.6	**5.6**	***8.5***	***-1.4***	***10.9***	-	-	-	-
46080	***-2.5***	**14.3**	***4.1***	36.1	**5.4**	***7.7***	***-1.7***	***11.5***	-	-	-	-
46082	**-6.2**	**14.5**	***-2.3***	37.4	**6.6**	***8.2***	***-5.1***	***11.0***	-	-	-	-
46083	**-2.5**	**14.6**	**9.4**	44.6	**8.5**	**9.9**	**-1.5**	**13.8**	-	-	-	-
46084	**0.3**	**14.5**	**12.8**	52.2	**7.7**	**8.9**	**-1.6**	**12.7**	-	-	-	-
46105	**-1.3**	25.1	**16.4**	71.8	**1.6**	**11.1**	23.8	27.7	***-4.2°***	52.6°	20.6	***20.9***
46107	28.2	38.1	97.6	181.8	**6.5**	**10.7**	11.2	22.9	***-1.9***	22.7	34.0	***17.1***

374

4 Resource characterization

IEC-TS recommends developing maps of the six characterization parameters as aids for project siting and planning (Section 4.1). Aggregation of the statistics of wave hindcast results over study areas are used to describe the seasonal variability of the resource and to compare the characteristics of different regions (Section 4.2). Finally, a long-term trend analysis, as suggested by IEC-TS, is performed to examine the variability of the resource at decadal scales (Section 4.3).

4.1 Spatial variability of the resource

To visualize the spatial variability of the resource, the 32-year average of all six wave resource parameters was computed at every node (internally at runtime in SWAN) and presented in Fig. 6. In general terms, the coastline exposed to the Pacific Ocean has larger average H_{m0} and J than the coastline facing the Bering Sea. In the southern Bering Sea, the sea states are milder and decrease eastwards from the western Aleutian Islands toward Bristol Bay. The energy period has a similar spatial distribution—longer period waves on the Pacific coast and shorter waves on the Bering Sea coast.

The θ_{Jmax} away from the Pacific coast responds to the majority of the energy approaching from the southwest. As waves approach the shore they turn toward the north. In the southeastern part of the Gulf of Alaska (colloquially known as the Alaska Panhandle) the waves are predominantly from the west-southwest, similar in direction and power to waves offshore of the U.S. Pacific Northwest [14] and British Columbia [42]. In the St. George and Bowers Basins and Bristol Bay, θ_{Jmax} is predominantly from the north. This implies that a significant portion of the swell energy arriving from the Pacific Ocean is dissipated on the southern coast of the Aleutian Arc. However, some energy from the Pacific Ocean does travel into the Bering Sea. To

illustrate this, the wave spectrum is averaged at selected stations around the study area and shown in Fig. 7, where hotter colors indicate more energy. Stations 6 – 8 show that most of the most energetic sea states approach from the south-southwest corresponding to Pacific Ocean swell. However, there is transmission from waves generated in the Bering Sea into the Pacific Ocean as seen in Station 5 which shows a secondary peak (in terms of total energy) at 10 s from the North-Northeast.

The directionality coefficient increases eastward and shoreward (Fig. 6f). The low directionality coefficient in the Aleutian Islands responds to the exposure of this region to multiple swell directions. The averaged spectra offshore and southward of the Aleutian Islands show energy approaching from the southeast and from the north (Fig. 7 stations 4 and 5). Seasonal maps showing the monthly and inter-annual variability of these parameters were presented in the study report [60].

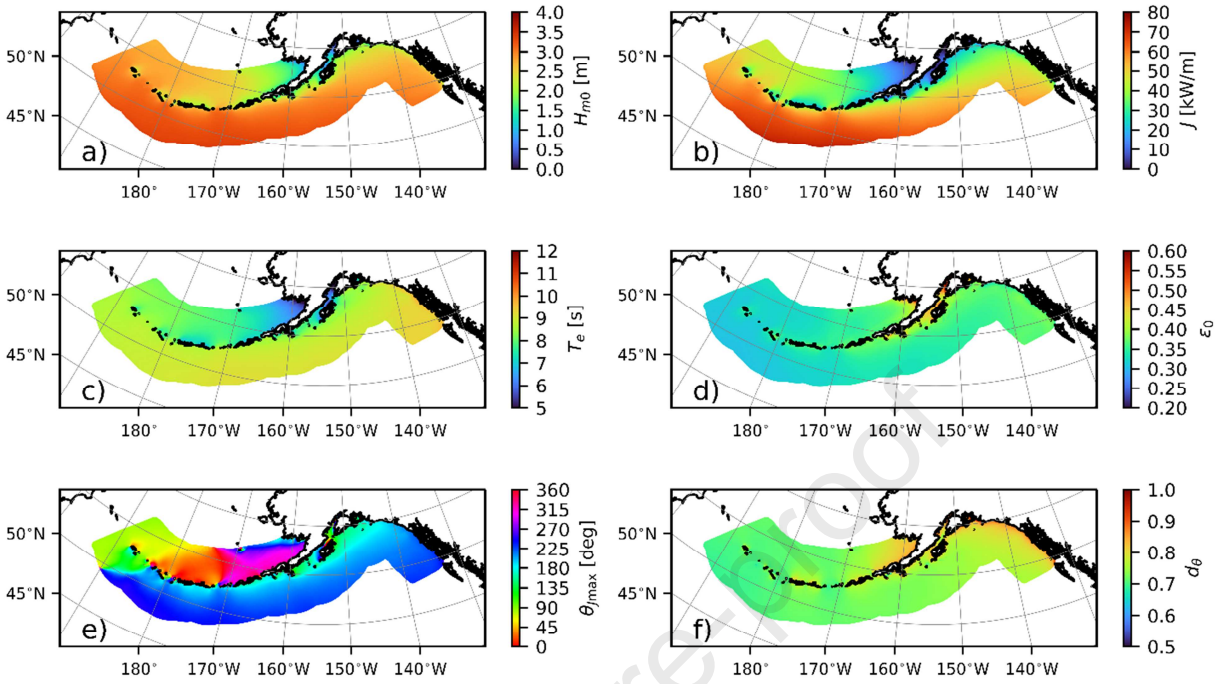

410

411 Fig. 6. Simulated 32-year averaged (a) significant wave height, (b) omnidirectional wave
412 power, (c) energy period, (d) spectral width, (e) direction of maximum directionally resolved
413 wave power, and (f) directionality coefficient for the southern Alaska coast.

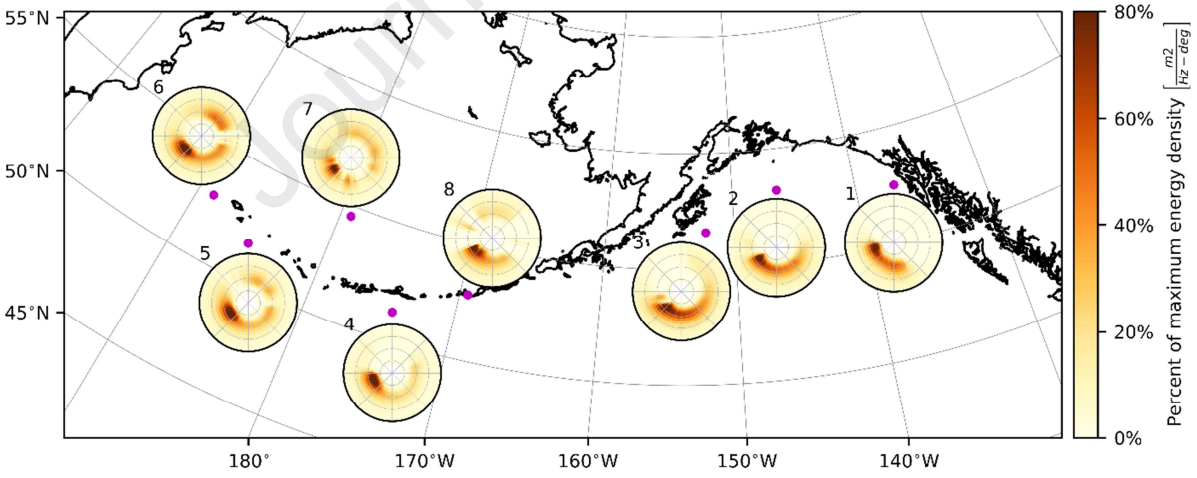

414

415 Fig. 7. Averaged wave spectra at selected locations. In the radial direction, concentric circles
416 are drawn at 0.05, 0.10, 0.15, and 0.20 Hz. Hotter colors indicate a more energetic sea state.
417 Color scales are normalized to emphasize distributions.

4.2 Regional analysis and aggregated results

Aggregation of model results gives developers information about the general wave climate of different regions. To perform these aggregations, six regions have been delineated as shown in Fig. 8. The Aleutian Islands are exposed to two different wave climates in their northern and southern coasts. Thus, these two coasts are analyzed separately, and results are aggregated in the St George and Bowers Basin for the north facing regions and the Aleutian Arc for the south facing regions. Bristol Bay, which is mostly exposed to the Bering Sea is aggregated as a unique region. On the south side, the Alaska Peninsula is treated independently from the Aleutian Arc because the peninsula blocks waves that approach from the Bering Sea. Further to the east Kodiak and the Gulf of Alaska are treated independently and the boundaries were selected rather arbitrarily. The wave resource is evaluated using model results collected every 10 km at an isoline 20 km from shore. Note that a similar analysis could have been performed based on water depth, but the distance from the coast will vary from point to point. Thus, this analysis provides information about the general wave power arriving at a practical distance from shore.

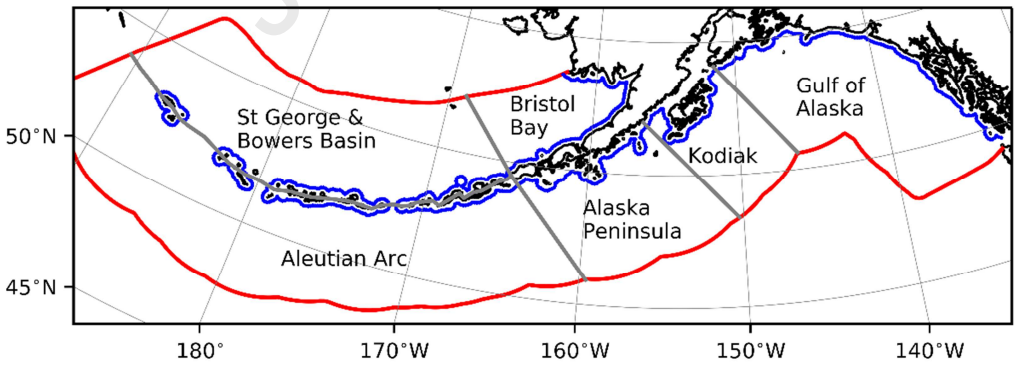

Fig. 8. Regions for wave resource aggregation. Stations 20 km from shore are outlined in blue. The wave model domain is outlined in red.

4.2.1 Statistics of resource parameters

Statistics for the six IEC parameters are computed at each node along the 20 km from shore isoline (shown in Fig. 8) based on the 3-hourly output over the 32 years of data. Then the arithmetic average of the points inside each of the regions is taken. Table 5 through Table 10 show the summarized statistics. Statistics for $\theta_{J_{max}}$ are omitted because means and percentiles of a periodic variable, where 0° and 360° represent the same condition, are not physically meaningful.

Table 5. Aggregated statistics for wave resource parameters 20 km offshore in the Gulf of Alaska.

Parameter	J [kW/m]	H_{m0} [m]	T_e [s]	ε_0 -	d -
Mean	31.2	2.2	9	0.37	0.84
Std Dev	40.3	1.1	1.5	0.09	0.08
10th percentile	5.3	1.1	7.2	0.26	0.74
50th percentile	16.9	2	8.9	0.35	0.85
90th percentile	73.6	3.8	11	0.5	0.92
Maximum	707.8	9.9	17.2	0.83	0.98
Minimum	1	0.5	4.3	0.19	0.38
Monthly Variability	42.7	1.5	1.4	0.09	0.04

Table 6. Aggregated statistics for wave resource parameters 20 km offshore of Kodiak.

Parameter	J [kW/m]	H_{m0} [m]	T_e [s]	ε_0 -	d -
Mean	20.0	1.9	7.5	0.41	0.79
Std Dev	29.3	1.0	1.5	0.11	0.12
10th percentile	2.8	0.9	5.7	0.28	0.60
50th percentile	10.1	1.7	7.4	0.39	0.82
90th percentile	46.7	3.2	9.6	0.56	0.92
Maximum	561.9	8.6	13.9	0.91	0.97
Minimum	0.6	0.4	4.1	0.20	0.38
Monthly Variability	31.8	1.4	1.1	0.14	0.08

Table 7. Aggregated statistics for wave resource parameters 20 km offshore of the Alaska Peninsula.

Parameter	J [kW/m]	H_{m0} [m]	T_e [s]	ε_0 -	d -

Mean	28.2	2.2	8.0	0.40	0.77
Std Dev	43.0	1.1	1.5	0.10	0.12
10th percentile	4.4	1.1	6.1	0.28	0.59
50th percentile	14.0	1.9	7.9	0.38	0.80
90th percentile	64.9	3.7	10.0	0.54	0.90
Maximum	825.7	10.2	14.7	0.84	0.96
Minimum	1.0	0.5	4.4	0.20	0.36
Monthly Variability	45.2	1.6	1.3	0.12	0.08

Table 8. Aggregated statistics for wave resource parameters 20 km offshore of the Aleutian Arc.

Parameter	J [kW/m]	H_{m0} [m]	T_e [s]	ε_0 -	d -
Mean	45.4	2.8	8.6	0.34	0.75
Std Dev	62.9	1.3	1.6	0.07	0.12
10th percentile	7.0	1.4	6.7	0.26	0.57
50th percentile	24.4	2.5	8.4	0.33	0.77
90th percentile	104.3	4.6	10.6	0.44	0.89
Maximum	1041.9	11.8	15.9	0.70	0.91
Minimum	1.8	0.7	4.8	0.19	0.36
Monthly Variability	79.5	2.1	2.2	0.08	0.08

Table 9. Aggregated statistics for wave resource parameters 20 km offshore of the St. George and Bowers Basins.

Parameter	J [kW/m]	H_{m0} [m]	T_e [s]	ε_0 -	d -
Mean	31.7	2.4	7.6	0.35	0.75
Std Dev	48.0	1.3	1.6	0.08	0.13
10th percentile	3.4	1.0	5.7	0.26	0.56
50th percentile	16.6	2.1	7.4	0.33	0.78
90th percentile	74.1	4.0	9.7	0.45	0.90
Maximum	770.3	10.6	14.1	0.74	0.96
Minimum	0.9	0.5	4.1	0.20	0.37
Monthly Variability	56.9	2.0	2.4	0.08	0.08

Table 10. Aggregated statistics for wave resource parameters 20 km offshore of Bristol Bay.

Parameter	J [kW/m]	H_{m0} [m]	T_e [s]	ε_0 -	d -
Mean	11.3	1.4	6.3	0.40	0.83
Std Dev	20.1	0.8	1.5	0.11	0.12
10th percentile	1.1	0.6	4.5	0.28	0.64
50th percentile	5.2	1.2	6.0	0.37	0.87
90th percentile	26.8	2.5	8.3	0.55	0.95
Maximum	402.9	7.7	13.8	0.93	0.98
Minimum	0.1	0.2	2.9	0.21	0.39

Monthly Variability	18.2	1.0	1.5	0.09	0.08

458

459 The omnidirectional wave power has a maximum mean value (45.4 kW/m) offshore of
460 the Aleutian Arc and decreases eastward reaching a minimum offshore of Kodiak (20 kW/m),
461 where the resource is 56% smaller. However, the mean J increases offshore of the Gulf of Alaska
462 and has a value of 31 kW/m. These values are similar in magnitude to those offshore of the U.S.
463 Pacific Northwest [14]. The mean J is 30% smaller in the St. George and Bowers Basin, and
464 75% smaller in Bristol Bay, compared to the maximum mean J in the Aleutian Arc. The high
465 wave power in the Aleutian Arc is also accompanied by the highest monthly variability. Both the
466 H_{m0} and T_e show patterns similar to J, which could be expected, although not necessarily,
467 because the latter is directly proportional to the former two variables. The most directionally
468 uniform waves are found in the Gulf of Alaska and Bristol Bay, because these regions are not
469 exposed to multi-directional swells like the Aleutian Arc.

470 Histograms of significant wave height and energy period are required by IEC-TS 62600-
471 101 to characterize the resource because many devices are tuned to respond preferentially to a
472 range of H_{m0} and T_e values. Regionally averaged bivariate distributions are presented in Fig. 9.
473 To satisfy the IEC-TS requirements, the histograms must have 0.5 m H_{m0} and 1 s T_e bins. Data
474 are binned using the time series for all points inside the region domains. The most apparent trend
475 is a westward shift toward shorter periods starting in the Gulf of Alaska. In addition, three
476 distinct shapes of the distributions can be observed, one for the Pacific-facing regions, another
477 for the St. George and Bowers Basins, and one for Bristol Bay. The St. George and Bowers
478 Basins do not experience long swells (T_e > 14 s) at less than 5 m H_{m0} like the Pacific-facing
479 regions do. Finally, waves in Bristol Bay are both shorter and smaller than in the rest of the study
480 region.

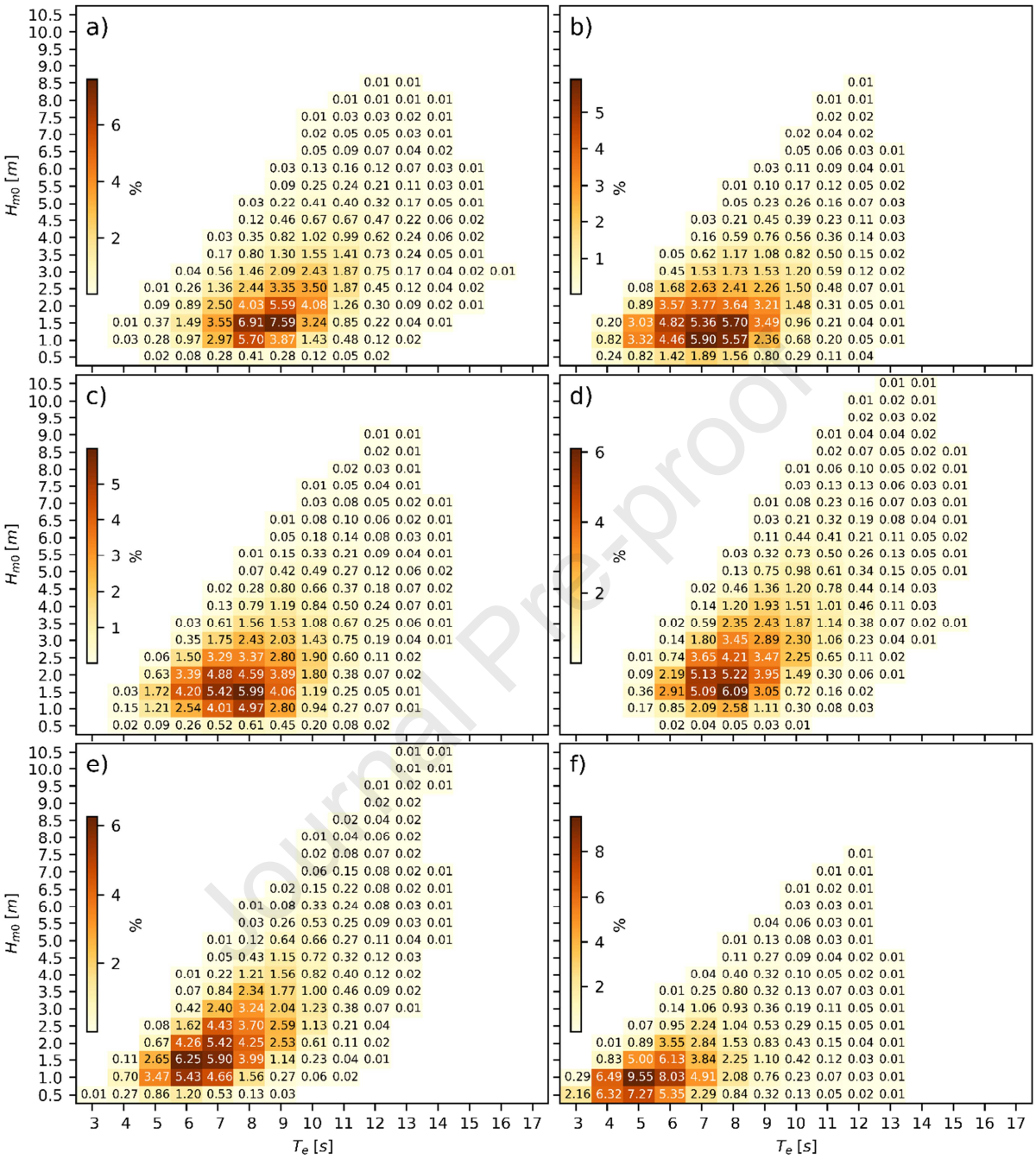

Fig. 9. Bivariate distribution of significant wave height and energy period in (a) the Gulf of Alaska; (b) Kodiak; (c) the Alaska Peninsula; (d) the Aleutian Arc; (e) St. George and Bowers Basins; and f) Bristol Bay.

4.2.2 Seasonal variability

The seasonal variability of the wave resource is relevant for energy production forecasting and device tuning. The cumulative distribution functions of monthly averaged omnidirectional wave power are shown in Fig.10. All regions show seasonal variability on the order of 50 kW/m at the 50th percentile; the Aleutian Arc is the most energetic region and Bristol Bay the least. All regions have energetic late autumns and winters, and calmer summers. In Bristol Bay, the most energetic months are October–December, while for other regions November–January is the most energetic trimester. During the late winter sea ice covers a large portion of the Bering Sea, thus reducing the fetch available for wave development, and during the summer the winds are weaker over the Bering Sea. A shorter shoulder regime is observed for the Gulf of Alaska in the months of May and September. This short transition between calmer and more energetic months is similar to that observed in the Pacific Northwest [14].

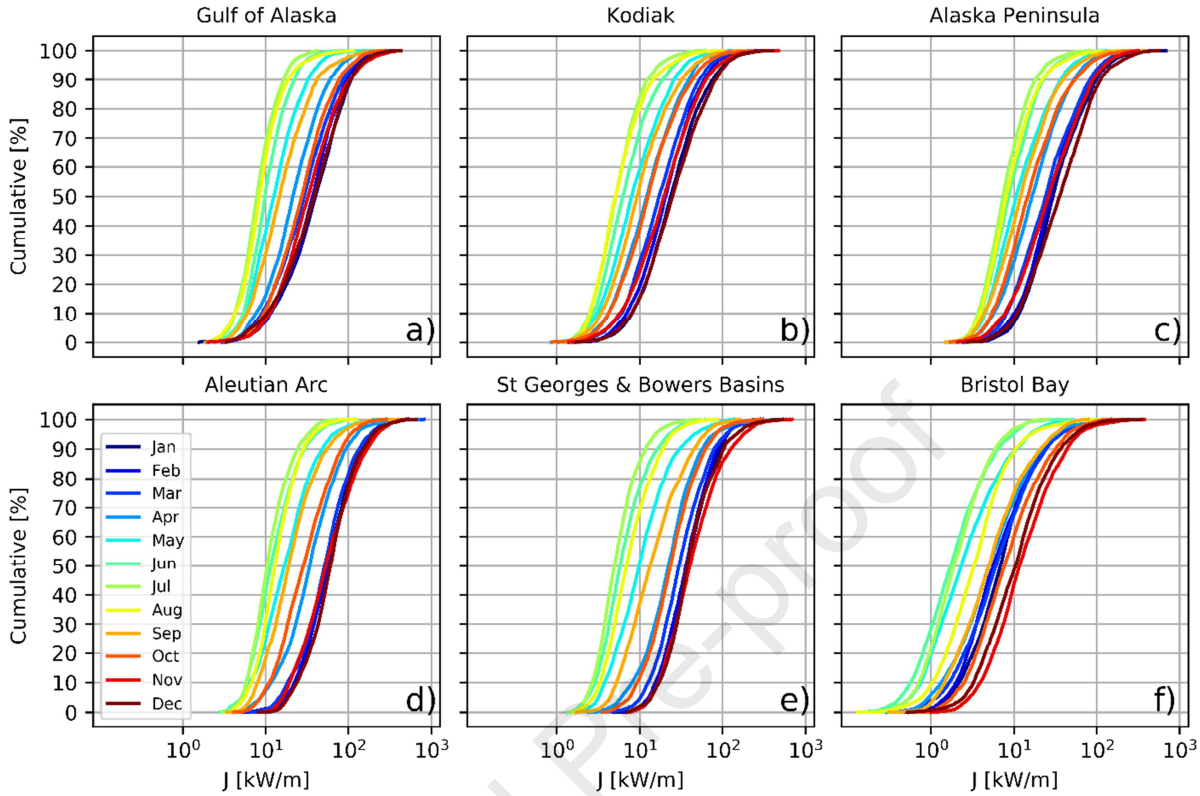

Fig.10. Spatially averaged cumulative distribution function of monthly averaged omnidirectional wave power in the six regions at 20 km from shore.

To complement the cumulative distribution functions, the IEC-TS 62600-101 recommends reporting the monthly variability of the resource for selected statistical parameters. The mean, 10th, 50th, and 90th percentiles of the omnidirectional wave power were computed and are shown in Fig. 11. For all regions, the mean exceeds the median (50th percentile) J, thereby showing the influence of the large events represented by the 90th percentile. The Aleutian Arc has the most energetic climate with large events averaging over 150 kW/m from November through February, as indicated in Fig. 11.

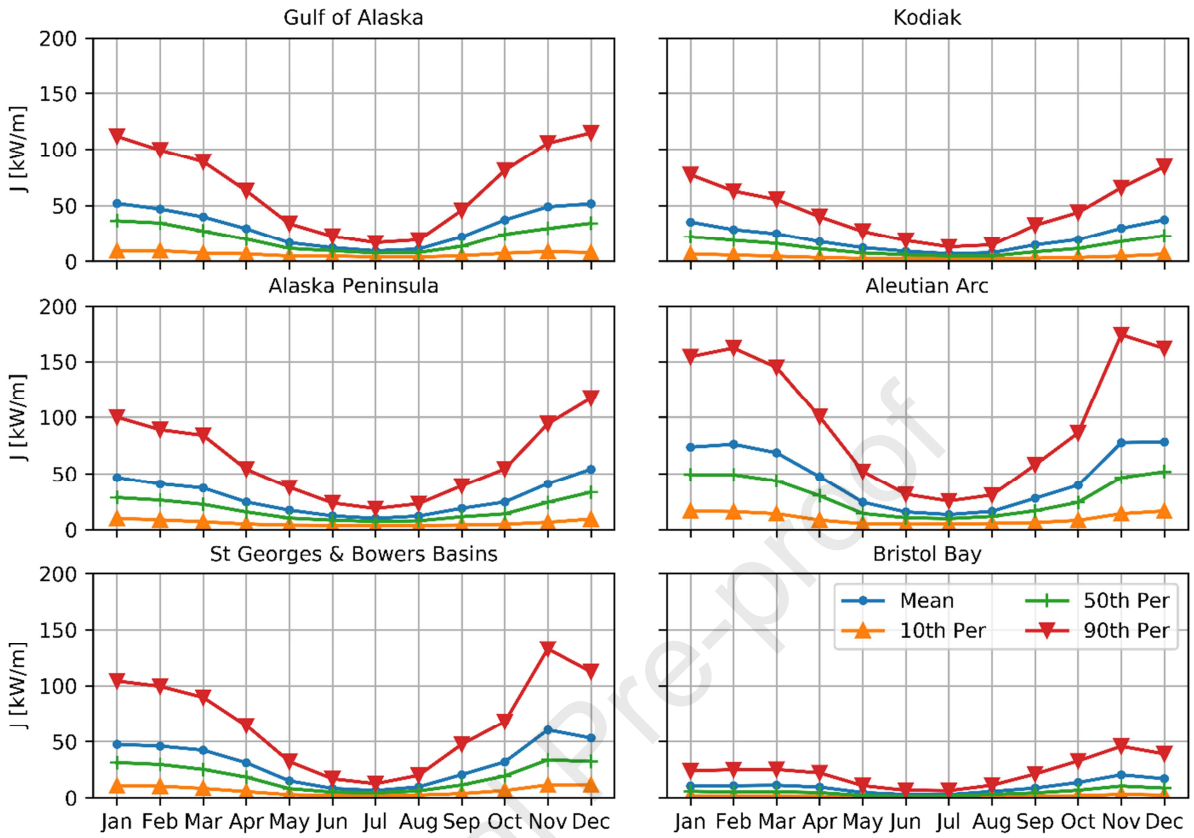

Fig. 11. Monthly averaged omnidirectional wave power computed 20 km from shore and aggregated over regions.

4.3 Decadal trends

Multi-decadal hindcasts allow the assessment of the uncertainty of long-term wave power. The IEC-TS recommends assessment of the variability of the wave power based on 3-, 5-, and 10-year moving averages. As an example, the ratio of the 5-year averaged omnidirectional wave power to the 32-year average is shown in Fig. 12. Kodiak and Bristol Bay are excluded from the figure because they show trends very similar to the Gulf of Alaska and St. Georges and Bowers Basins, respectively. During the second part of the 1980s, a positive anomaly reached values of over 7.5% for three consecutive years and close to 15% at its peak for the Eastern North Pacific Ocean. During that time period, the St. Georges and Bowers Basins also showed a positive anomaly, but at values less than 5%. Throughout the rest of the hindcast period the

anomalies are contained within ±10% with a couple of exceptions. It is important to note that in other areas of the northern Pacific Ocean it has been suggested that lower frequency oscillations, with periods longer than our hindcast period, might affect the wave power [72], thus Fig. 12 might only show parts of a longer cycle.

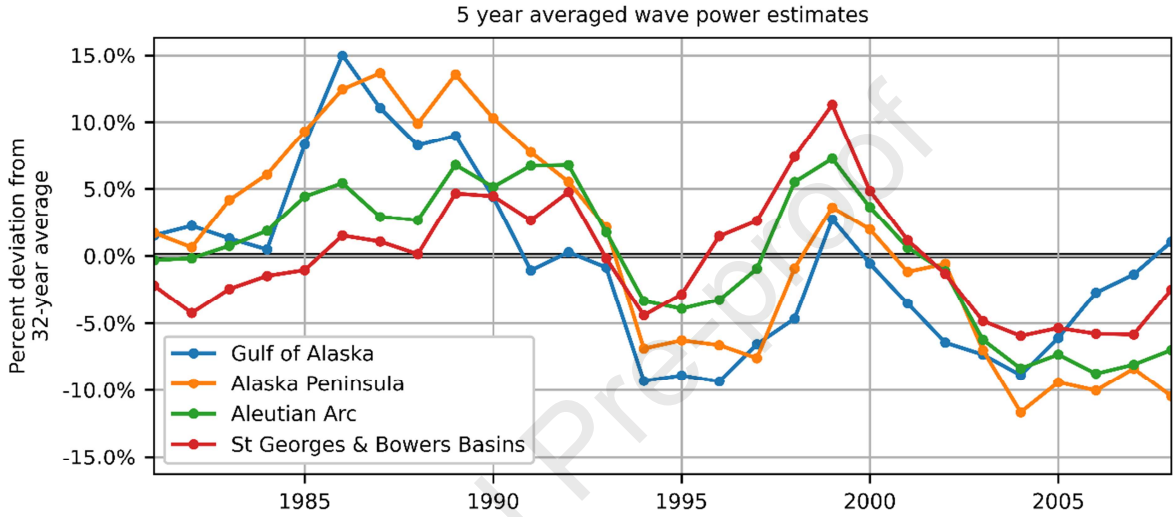

Fig. 12. Percent deviation from the 32-year averaged wave power using a 5-year moving average.

The El Niño Southern Oscillation (ENSO) has been linked to anomalies in the oceanographic conditions in regions of Alaska. For instance, it has been found that during ENSO years there are increased sea levels and anomalous circulation patterns in the Gulf of Alaska [73,74]. ENSO has also been linked to the variability in the sea ice cover of the Bering Sea [75], which would have an effect on the fetch for wave growth. This drives the investigation of the correlation between anomalous wave power and ENSO in the region. The Oceanic Niño Index (ONI) is a NOAA-defined indicator that correlates with El Niño and La Niña events. The ONI is defined as the 3-month running average of sea surface temperature anomalies in the region bounded by 5°S – 5°N and 120°W – 170°W. The ONI is shown in Fig. 13a-b with the yearly *J* anomaly in the six different analysis regions. The yearly *J* anomaly is computed by subtracting

538 the yearly averaged J from the 32-year averaged J. Correspondence between the signals is not
539 immediately clear when looking at the superimposed graphs. To investigate further, the 3-month
540 running averaged J anomaly is evaluated for correlation with ONI. For this analysis, the monthly
541 averaged J for each month is subtracted and normalized by the 32-year averaged J for that same
542 month, then a three-month running average, to follow the way the ONI is computed, is
543 performed. Cross correlations for each region are shown in Fig. 13c-h. The signals in the Gulf of
544 Alaska and Kodiak show statistically significant correlations with a 95% confidence level at 0.22
545 and 0.24, respectively, with a 3-month time lag. This follows the trend of lower correlations
546 between ONI and wave power anomaly in the poleward direction for western North America
547 (refer to Yang et al. [14] for a similar analysis of the U.S. West Coast). No statistically
548 significant correlations were found in the other analysis regions. Similar comparisons (not
549 shown) were performed using the Arctic Oscillation, for which no statistically significant
550 correlations were found, and with the Pacific-North America (PNA) index, which had similar
551 results to ONI with a 1-month time lag. Using results from a global hindcast, Reguero et al. [76]
552 found small correlations of wave power with the PNA index offshore of southern Alaska and did
553 not find correlations with 11 other indices. ONI was not analyzed in that study.

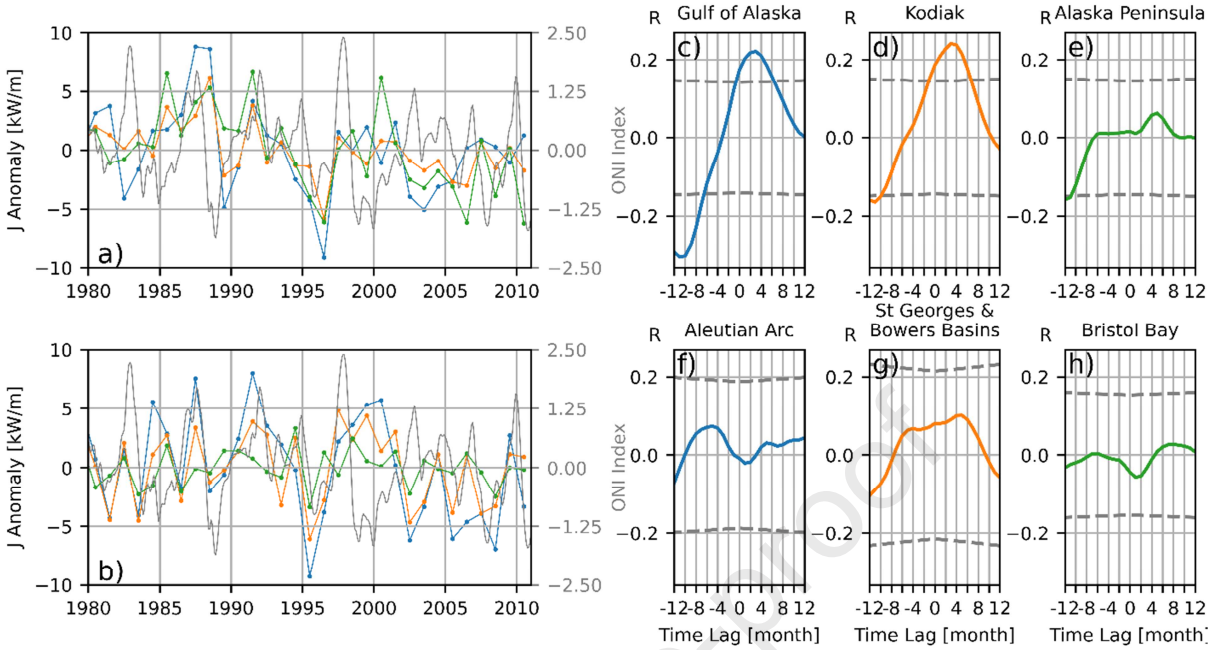

554

555 Fig. 13. (a-b) Yearly omnidirectional wave power anomaly for the six analysis regions (three
556 per panel) and the ONI value (https://www.cpc.ncep.noaa.gov/data/indices/oni.ascii.txt)
557 shown in gray with the scale on the right vertical axis. (c-h) Time lagged cross-correlations
558 between ONI and monthly wave power anomaly. The time series in (a) are color coded
559 relative to panels c, d, and e. The second row is equally color coded. Confidence levels at
560 95% are shown as dashed lines based on a Fisher's distribution.

561 **5 Nearshore wave resource**

562 The analysis presented in Section 4 focused on the incoming wave energy of Alaska.
563 However, shallow water features and exposure to the ocean based on coastline orientation also
564 play a significant role in the distribution of the resource [e.g. 14]. The nearshore resource
565 evaluation is based on output collected at virtual stations 5 km apart at 1 km from shore along all
566 the coastlines in the entire model domain.

567 The performance of WECs is significantly affected by the temporal variability of the
568 resource [77], so it is desirable to characterize the variability of the resource before deploying the
569 device. The MVI, SVI, and AVI serve to describe the wave resource variability at different
570 scales. Maps of these parameters computed at the 3570 analysis locations 1 km from shore are

shown in Fig. 14a-c. Hotter (cooler) colors indicate higher (lower) temporal variability. In general, the variability at the monthly scale is larger than that at the seasonal and yearly scales. The MVI value is highest in Prince William Sound and on the Bering Sea coast from the middle of the Alaska Peninsula to the west. The Pacific coast, which has the largest average wave power (see Fig. 6a), also has the lowest MVI value on the order of 1.5. The MVI value is generally lower in Bristol Bay, which is also a region of low wave power. In general, the SVI follows a similar pattern to the MVI.

Suitable locations for wave energy extraction require available power in addition to low variability of the wave resource. The OHI can be used to identify locations suitable for energy development based on average available power, the probability of occurrence of extractable power (at least 2 kW/m), and low monthly variability. Fig. 14d shows OHI computed for the nearshore stations. The eastern half of the Gulf of Alaska (locations east of ~145°W) has many locations with OHI values greater than 15 kW/m. Other regions with high OHI values are the Pacific Coast of the Aleutian Archipelago, a few stations around Kodiak, and the Alaska Peninsula. However, on the northern shore of the Aleutian Islands and western Alaska Peninsula there are many places where the OHI values exceed 5 kW/m, which is still significant in a global context. For reference, the OHI value at nearshore locations around China ranged from 1–4.5 [50] and from 1–5 in India [68].

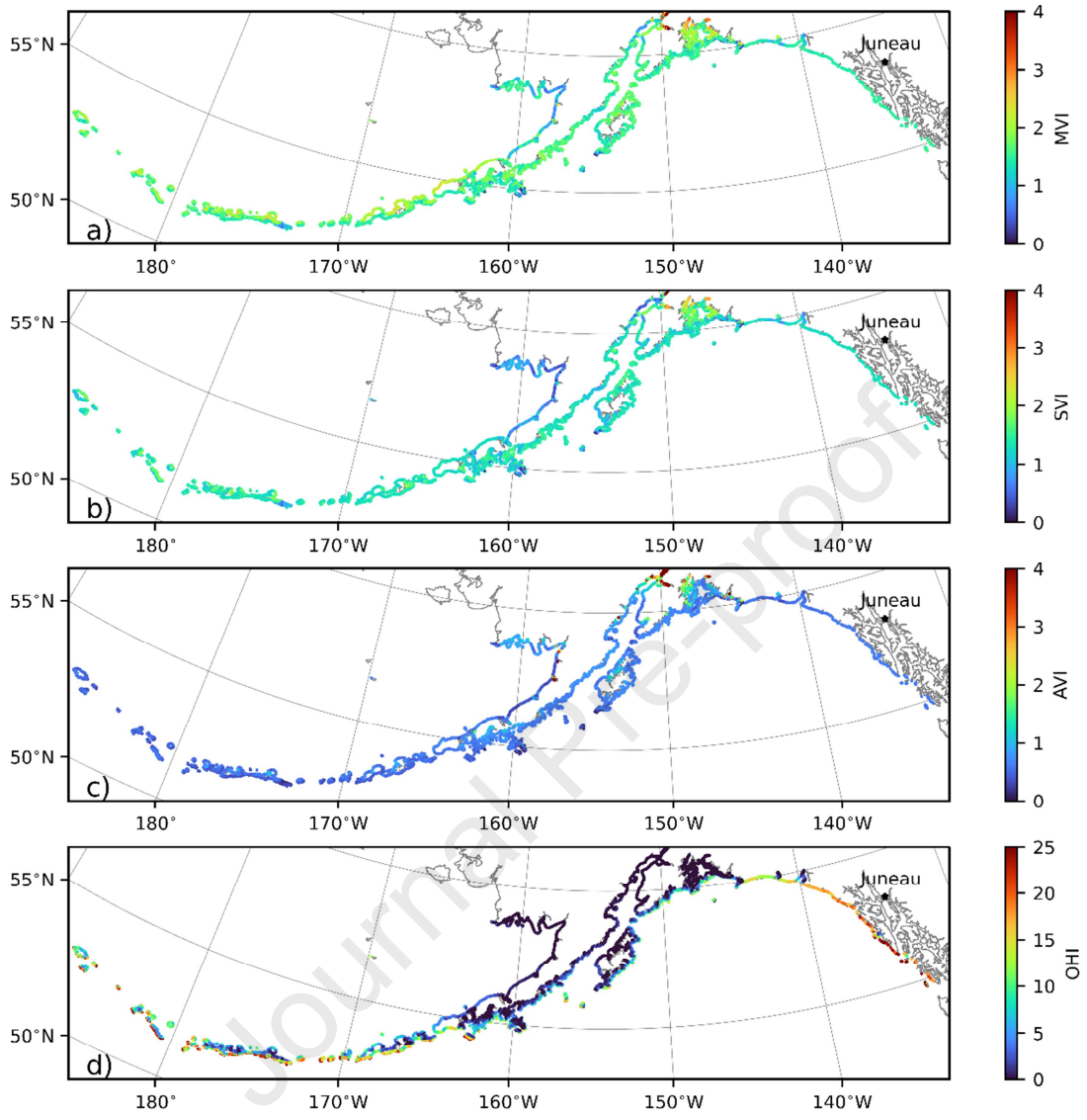

589

590 Fig. 14. (a) Monthly Variability Index, (b) Seasonal Variability Index, (c) Annual Variability
591 Index, and (d) Optimum Hotspot Identifier at points 1 km from shore.
592

593 The Eastern Gulf of Alaska and the Aleutian Arc have the largest number of nearshore
594 hotspots suitable for wave energy extraction. Of the 3570 analysis points, 991 have an OHI value
595 greater than 5 kW/m representing 28% of the analyzed points. Because we performed the
596 evaluation by comparing points equidistant from the coast, the depth variability of these hotspots
597 has not been quantified. For that purpose, the depth distribution of the locations with OHI values

598 greater than 5 kW/m is shown in Fig. 15. There is large variability in the water depth—most is
599 distributed between 10 and 60 m. This large diversity in water depth so close to shore positions
600 Alaska as a suitable place for testing and deploying different WEC technologies.

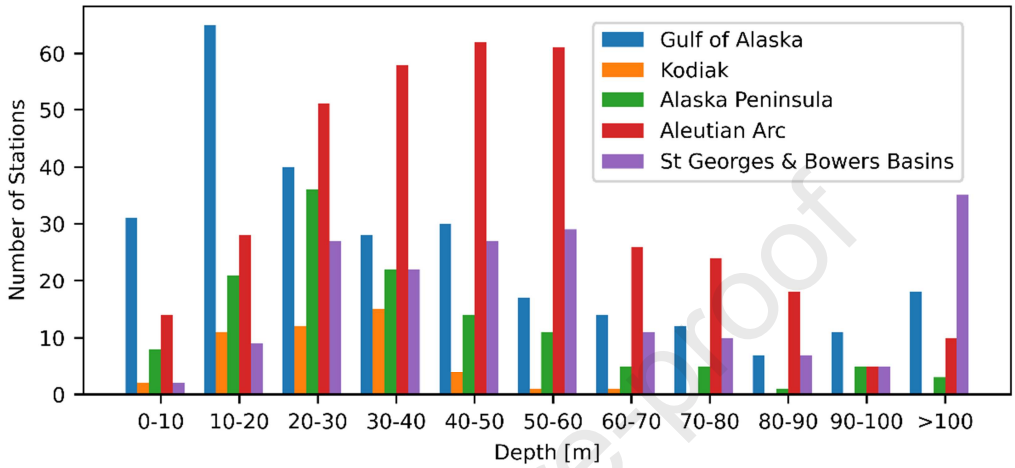

601

602 Fig. 15. Depth distribution of nearshore hotspots 1 km from shore and with Optimum
603 Hotspot Identifier values > 5 kW/m.

604 In addition to the OHI, wave power roses provide information about the directional
605 distribution of the resource at those locations and are shown in Fig. 16. This information is
606 relevant for directionally sensitive devices for which device performance is affected by the
607 alignment of the device with the incident wave directions. For instance, locations on the east and
608 west coasts of the Aleutian Islands that have high OHI values are subject to a more directionally
609 spread wave resource. In some cases, the stronger resource can arrive from both the Pacific
610 Ocean and the Bering Sea (see hotter colors). In the eastern Gulf of Alaska, the directionality of
611 the resource is reduced, and the maximum wave power arrives at directions within 67.5°.

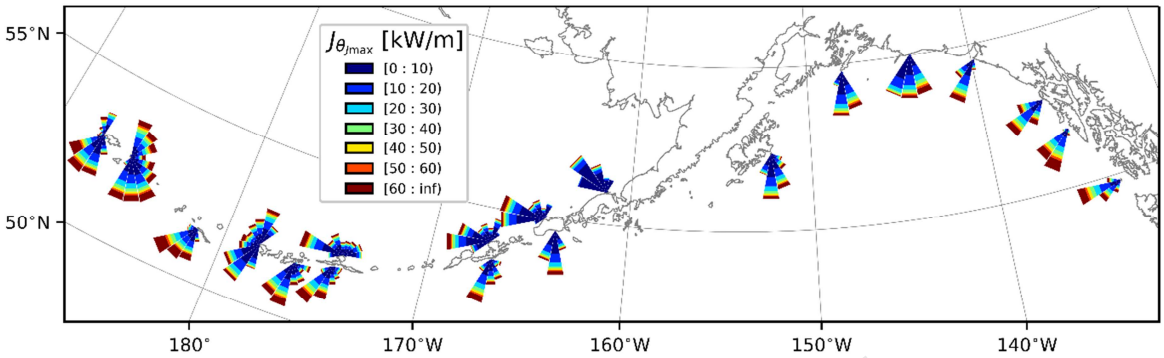

612

613 Fig. 16. Directionally resolved wave power roses at selected points located 1 km from shore
614 and that have OHI values greater than 5 kW/m. Directions are aggregated over 22.5° bins.

615 **6 Conclusions**

616 This study presents a characterization of the wave energy resource in southern Alaska
617 covering the EEZ with emphasis on the region 20 km or less from the shore. A high-resolution,
618 unstructured-grid SWAN was developed and validated against in situ measurements from 18
619 NDBC buoys. A 32-year hindcast covering the period from 1979 to 2010 was generated. The six
620 IEC-TS parameters for wave resource assessment were stored with a three-hourly interval over
621 the entire computational domain. Data from this hindcast can be downloaded free of charge from
622 the Amazon Web Services Open Data (https://registry.opendata.aws/wpto-pds-us-wave/), a
623 database maintained by the U.S. Department of Energy's National Renewable Energy
624 Laboratory.

625 A wave resource characterization based on aggregated statistics derived using the IEC-TS
626 62600-101 methodology showed that the wave resource is high and exhibits significant monthly
627 variability. The regions of Alaska exposed to the North Pacific Ocean were found to have the
628 largest wave resource. The Aleutian Islands have the maximum resource with an annual average
629 power of 46.5 kW/m on their southern coast. The directionality of the resource is highly

630 dependent on location. The eastern Gulf of Alaska has a lower directional distribution of the
631 resource because only swells from the west and south arrive at that coast. In contrast, locations
632 on the eastern and western coasts of the Aleutian Islands experience waves from many locations,
633 including waves propagating from the Bering Sea. Wave power anomalies in the Gulf of Alaska
634 and Kodiak were found to correlate with the ONI.

635 A nearshore wave resource characterization was performed at virtual stations located 1
636 km from shore. The monthly variability of the resource was found to be dependent on location.
637 When aggregated, 80% of the nearshore stations have an MVI value of between 1.2 and 2.0. The
638 OHI value was computed to identify suitable nearshore locations for wave energy extraction.
639 Close to 28% of the evaluated nearshore (1 km from shore) stations had OHI values greater than
640 5 kW/m at water depths that ranged from a few meters to over 100 m. The nearshore resource is
641 found to be suitable for extraction at many nearshore locations around the southern coast of
642 Alaska.

643

7 Acknowledgments

This study was funded by the U.S. Department of Energy, Office of Energy Efficiency and Renewable Energy, Water Power Technologies Office under contract DE-AC05-76RL01830 to Pacific Northwest National Laboratory (PNNL). All model simulations were performed using PNNL's Institutional Computing facility. The authors thank the external steering committee, chaired by Dr. Bryson Robertson, for providing technical oversight for input to and review of this model study. The authors thank two anonymous reviewers for providing detailed comments that resulted in an improved manuscript.

Appendix A: Additional error statistics

Commonly used error metrics used to evaluate the model performance for non-directional parameters are the root-mean-square-error (RMSE), mean percentage error (PE), scatter index (SI), bias (b), and the linear correlation coefficient (R):

$$RMSE = \sqrt{\frac{\sum_{i=1}^{N}(P_i - M_i)^2}{N}} \tag{A1}$$

$$PE = \frac{100}{N}\sum_{i=1}^{N}\frac{P_i - M_i}{M_i} \tag{A2}$$

$$SI = \frac{RMSE}{\overline{M}} \tag{A3}$$

$$bias = \frac{1}{N}\sum_{i=1}^{N} P_i - M_i \tag{A4}$$

$$\mathrm{R} = \frac{\sum_{i=1}^{N}\left(P_i - \overline{P}\right)\left(M_i - \overline{M}\right)}{\sqrt{\left[\sum_{i=1}^{N}\left(P_i - \overline{P}\right)^2\right]\left[\sum_{i=1}^{N}\left(M_i - \overline{M}\right)^2\right]}} \tag{A5}$$

where N is the number of measurements, M_i is the measured data, P_i is the predicted results, and overlines represent time averages. The directional performance is evaluated following the Hanson et al. [78] method by computing the angular bias (b_θ) [79] and the circular correlation (R_θ):

$$bias_\theta = \tan^{-1}\frac{\sum_{i=1}^{N}\sin|P_i - M_i|}{\sum_{i=1}^{N}\cos|P_i - M_i|} \tag{A6}$$

$$\mathrm{R}_\theta = \frac{\sum_{i=1}^{N}\sin\left(P_i - \overline{P}\right)\sin\left(M_i - \overline{M}\right)}{\sqrt{\left(\sum_{i=1}^{N}\left[\sin\left(P_i - \overline{P}\right)\right]^2\right)\left(\sum_{i=1}^{N}\left[\sin\left(M_i - \overline{M}\right)\right]^2\right)}} \tag{A7}$$

The error statistics at the buoy stations (Fig. 5) are shown in Table A1, Table A2, and Table A3.

Table A1. Error statistics for significant wave height and omnidirectional wave power.

		H_{m0} (m)					J (kW/m)				
Buoy	N	RMSE	PE (%)	SI	bias	R	RMSE	PE (%)	SI	bias	R
46001	115,945	0.46	5.2	0.17	0.03	0.95	24.77	23.2	0.57	1.42	0.91
46060	131,181	0.27	7.3	0.38	-0.01	0.82	2.91	58.9	1.26	0.43	0.76
46061	171,964	0.43	15.5	0.27	0.14	0.92	13.93	52.5	0.95	2.75	0.86
46066	71,973	0.49	7.7	0.17	0.07	0.95	29.96	35.6	0.59	2.29	0.91
46070	19,868	0.44	1.0	0.17	-0.11	0.96	22.07	19.6	0.57	-1.92	0.94
46071	33,179	0.54	8.9	0.19	0.06	0.95	36.78	36.2	0.75	2.07	0.90
46072	50,650	0.57	5.8	0.19	0.01	0.93	36.64	26.2	0.67	-0.67	0.88
46073	41,176	0.42	10.9	0.18	0.11	0.96	20.81	33.9	0.65	2.38	0.92
46075	76,552	0.49	7.5	0.18	0.05	0.94	27.87	29.2	0.66	0.86	0.90
46076	31,177	0.41	11.1	0.20	0.05	0.95	17.38	54.1	0.74	1.12	0.91
46077	36,404	0.57	-22.5	0.48	-0.36	0.79	6.46	-11.7	1.15	-2.67	0.73
46078	38,104	0.49	4.9	0.18	0.01	0.94	24.13	21.9	0.56	0.11	0.90
46080	41,450	0.47	2.1	0.19	-0.09	0.94	18.42	15.6	0.57	-2.91	0.91
46082	43,444	0.55	-2.4	0.23	-0.20	0.94	28.40	6.3	0.79	-5.74	0.89
46083	58,820	0.47	4.1	0.20	-0.08	0.95	20.86	31.3	0.64	-2.15	0.90
46084	54,323	0.43	5.0	0.17	-0.01	0.96	23.11	29.1	0.57	-0.06	0.92
46105	3,411	0.72	-1.3	0.44	-0.24	0.81	17.75	25.4	1.24	-5.04	0.69
46107	16,321	0.35	33.2	0.36	0.21	0.88	5.62	19.7	1.033	2.32	0.85

Table A2. Error statistics for energy period and spectral width.

		T_e (s)					ϵ_0				
Buoy	N	RMSE	PE (%)	SI	bias	R	RMSE	PE (%)	SI	bias	R
46001	115,945	1.02	7.2	0.12	0.53	0.85	0.06	-0.8	0.16	-0.01	0.76
46060	131,181	2.25	27.6	0.34	1.40	0.57	0.16	5.4	0.40	-0.01	0.17
46061	171,964	1.22	8.1	0.15	0.50	0.72	0.08	-4.8	0.22	-0.03	0.64
46066	71,973	1.10	9.7	0.13	0.70	0.86	0.06	2.3	0.17	0.00	0.67
46070	19,868	1.02	11.5	0.14	0.78	0.90	0.06	7.0	0.19	0.02	0.57
46071	33,179	0.98	8.2	0.12	0.59	0.88	0.06	6.4	0.18	0.02	0.67
46072	50,650	1.00	6.0	0.12	0.44	0.84	0.05	0.2	0.17	0.00	0.65
46073	41,176	0.70	4.2	0.09	0.27	0.90	0.06	10.8	0.19	0.03	0.78
46075	76,552	0.93	6.6	0.11	0.48	0.88	0.06	2.3	0.17	0.00	0.71
46076	31,177	1.37	14.2	0.18	0.89	0.76	0.09	16.4	0.29	0.04	0.49
46077	36,404	1.81	22.3	0.33	0.87	0.43	0.20	59.5	0.67	0.13	-0.12
46078	38,104	0.91	6.1	0.11	0.43	0.86	0.05	0.3	0.15	0.00	0.77
46080	41,450	0.90	5.9	0.11	0.39	0.82	0.06	1.8	0.17	0.00	0.75
46082	43,444	1.01	7.2	0.12	0.51	0.82	0.06	-3.6	0.17	-0.02	0.77
46083	58,820	1.31	12.3	0.16	0.86	0.81	0.08	3.2	0.22	0.00	0.60
46084	54,323	1.24	11.1	0.15	0.80	0.84	0.07	3.6	0.19	0.01	0.68
46105	3,411	1.34	5.8	0.21	0.21	0.57	0.14	33.2	0.45	0.07	0.26
46107	16,321	1.27	5.7	0.16	0.37	0.64	0.10	17.2	0.32	0.04	0.51

Table A3. Error statistics for direction of maximum directionally resolved wave power and directionality coefficient.

	θ_{Jmax} (deg)			d				
Buoy	N	$bias_\Theta$	R_Θ	RMSE	PE (%)	SI	bias	R
46060	21,878	25.69	0.02	0.32	45.2	0.49	0.27	0.03
46105	3,411	30.17	0.51	0.21	22.2	0.32	0.12	0.05
46107	16,321	15.50	0.45	0.26	39.2	0.40	0.24	0.41

Model-data comparisons between CFSR and the wave buoys are shown in Table A4. The anemometers at the buoys are located between 3.8 and 5 m above sea level. The wind speed at 10 m is estimated following the wind profile power law with power 1/7, typically used for stable atmospheric conditions.

Table A4. CFSR model performance at ocean buoys from 2005 to 2010.

	Wind Speed (m/s)						Wind Direction (deg)	
Buoy	N	RMSE	PE (%)	SI	bias	R	$bias_\Theta$	R_Θ
46001	36,553	1.5	13.1	0.18	-0.10	0.93	11.5	0.94
46060	46,737	3.4	22.4	0.58	-1.35	0.62	19.7	0.44
46061	68,171	3.0	11.9	0.41	-1.43	0.83	14.9	0.59
46066	28,592	1.4	1.1	0.16	-0.47	0.95	9.2	0.96
46070	19,372	1.6	5.8	0.17	-0.44	0.94	10.1	0.93
46071	29,773	1.7	13.4	0.20	0.27	0.93	12.5	0.93
46072	16,855	1.7	11.9	0.19	-0.35	0.93	12.9	0.95
46073	44,342	1.9	-4.2	0.19	-1.04	0.94	10.5	0.94
46075	38,415	1.8	16.2	0.19	-0.31	0.92	11.0	0.94
46076	32,702	2.1	18.1	0.30	-0.38	0.88	18.0	0.84
46077	29,901	3.8	8.3	0.48	-2.31	0.74	29.1	0.76
46078	34,423	2.0	29.7	0.23	-0.07	0.88	20.1	0.89
46080	20,637	2.7	82.1	0.34	0.06	0.81	16.5	0.89
46082	37,352	2.5	11.8	0.32	-1.22	0.91	17.6	0.81
46083	39,401	2.4	12.9	0.30	-0.94	0.89	17.5	0.80
46084	35,647	2.9	84.0	0.37	-0.33	0.79	16.9	0.82

References

[1] K. Gunn, C. Stock-Williams, Quantifying the global wave power resource, Renewable Energy. 44 (2012) 296–304. https://doi.org/10.1016/j.renene.2012.01.101.

[2] R.A. Arinaga, K.F. Cheung, Atlas of global wave energy from 10 years of reanalysis and hindcast data, Renewable Energy. 39 (2012) 49–64. https://doi.org/10.1016/j.renene.2011.06.039.

[3] A.M. Cornett, A global wave energy resource assessment, in: The Eighteenth International Offshore and Polar Engineering Conference, International Society of Offshore and Polar Engineers, 2008.
[4] I. Fairley, M. Lewis, B. Robertson, M. Hemer, I. Masters, J. Horrillo-Caraballo, H. Karunarathna, D.E. Reeve, A classification system for global wave energy resources based on multivariate clustering, Applied Energy. 262 (2020) 114515. https://doi.org/10.1016/j.apenergy.2020.114515.
[5] B. Robertson, Wave energy assessments: quantifying the resource and understanding the uncertainty, in: Marine Renewable Energy, Springer, 2017: pp. 1–36.
[6] G. Hagerman, G. Scott, Mapping and Assessment of the United States Ocean Wave Energy Resource, (2011). https://doi.org/10.2172/1219363.
[7] S. Ahn, K.A. Haas, V.S. Neary, Dominant Wave Energy Systems and Conditional Wave Resource Characterization for Coastal Waters of the United States, Energies. 13 (2020) 3041. https://doi.org/10.3390/en13123041.
[8] Z. Defne, K.A. Haas, H.M. Fritz, Wave power potential along the Atlantic coast of the southeastern USA, Renewable Energy. 34 (2009) 2197–2205. https://doi.org/10.1016/j.renene.2009.02.019.
[9] C. Ozkan, T. Mayo, The renewable wave energy resource in coastal regions of the Florida peninsula, Renewable Energy. 139 (2019) 530–537. https://doi.org/10.1016/j.renene.2019.02.090.
[10] P. Lenee-Bluhm, R. Paasch, H.T. \"Ozkan-Haller, Characterizing the wave energy resource of the US Pacific Northwest, Renewable Energy. 36 (2011) 2106–2119. https://doi.org/10.1016/j.renene.2011.01.016.
[11] G. García-Medina, H.T. Özkan-Haller, P. Ruggiero, Wave resource assessment in Oregon and southwest Washington, USA, Renewable Energy. 64 (2014) 203–214. https://doi.org/10.1016/j.renene.2013.11.014.
[12] Z. Yang, V.S. Neary, T. Wang, B. Gunawan, A.R. Dallman, W.-C. Wu, A wave model test bed study for wave energy resource characterization, Renewable Energy. 114 (2017) 132–144. https://doi.org/10.1016/j.renene.2016.12.057.
[13] W.-C. Wu, T. Wang, Z. Yang, G. García-Medina, Development and validation of a high-resolution regional wave hindcast model for U.S. West Coast wave resource characterization, Renewable Energy. 152 (2020) 736–753. https://doi.org/10.1016/j.renene.2020.01.077.
[14] Z. Yang, G. García-Medina, W.-C. Wu, T. Wang, Characteristics and variability of the nearshore wave resource on the U.S. West Coast, Energy. 203 (2020) 117818. https://doi.org/10.1016/j.energy.2020.117818.
[15] A. Beyene, J.H. Wilson, Digital mapping of California wave energy resource, International Journal of Energy Research. 31 (2007) 1156–1168. https://doi.org/10.1002/er.1326.
[16] A. Beyene, J.H. Wilson, Comparison of wave energy flux for northern, central, and southern coast of California based on long-term statistical wave data, Energy. 31 (2006) 1856–1869. https://doi.org/10.1016/j.energy.2005.08.008.
[17] M.F. Canals Silander, C.G. García Moreno, On the spatial distribution of the wave energy resource in Puerto Rico and the United States Virgin Islands, Renewable Energy. 136 (2019) 442–451. https://doi.org/10.1016/j.renene.2018.12.120.

[18] N. Li, K.F. Cheung, J.E. Stopa, F. Hsiao, Y.-L. Chen, L. Vega, P. Cross, Thirty-four years of Hawaii wave hindcast from downscaling of climate forecast system reanalysis, Ocean Modelling. 100 (2016) 78–95. https://doi.org/10.1016/j.ocemod.2016.02.001.

[19] J.E. Stopa, K.F. Cheung, Y.-L. Chen, Assessment of wave energy resources in Hawaii, Renewable Energy. 36 (2011) 554–567. https://doi.org/10.1016/j.renene.2010.07.014.

[20] J.E. Stopa, J.-F. Filipot, N. Li, K.F. Cheung, Y.-L. Chen, L. Vega, Wave energy resources along the Hawaiian Island chain, Renewable Energy. 55 (2013) 305–321. https://doi.org/10.1016/j.renene.2012.12.030.

[21] S.F. Barstow, O. Haug, H.E. Krogstad, Satellite altimeter data in wave energy studies, in: Ocean Wave Measurement and Analysis, ASCE, 1998: pp. 339–354.

[22] M. Previsic, Offshore wave energy conversion devices, Electric Power Research Institute (EPRI), Palo Alto, CA, USA, 2004.

[23] L. Kilcher, R. Thresher, Marine hydrokinetic energy site identification and ranking methodology part I: Wave energy, National Renewable Energy Lab.(NREL), Golden, CO (United States), 2016.

[24] L. Cavaleri, S. Abdalla, A. Benetazzo, L. Bertotti, J.-R. Bidlot, Ø. Breivik, S. Carniel, R.E. Jensen, J. Portilla-Yandun, W.E. Rogers, A. Roland, A. Sanchez-Arcilla, J.M. Smith, J. Staneva, Y. Toledo, G.Ph. van Vledder, A.J. van der Westhuysen, Wave modelling in coastal and inner seas, Progress in Oceanography. 167 (2018) 164–233. https://doi.org/10.1016/j.pocean.2018.03.010.

[25] IEC TS 62600-101, Marine energy - Wave, tidal and other water current converters - Part 101: Wave energy resource assessment and characterization, International Electrotechnical Commission, Geneva, Switzerland, 2015.

[26] J. Thomson, Y. Fan, S. Stammerjohn, J. Stopa, W.E. Rogers, F. Girard-Ardhuin, F. Ardhuin, H. Shen, W. Perrie, H. Shen, S. Ackley, A. Babanin, Q. Liu, P. Guest, T. Maksym, P. Wadhams, C. Fairall, O. Persson, M. Doble, H. Graber, B. Lund, V. Squire, J. Gemmrich, S. Lehner, B. Holt, M. Meylan, J. Brozena, J.-R. Bidlot, Emerging trends in the sea state of the Beaufort and Chukchi seas, Ocean Modelling. 105 (2016) 1–12. https://doi.org/10.1016/j.ocemod.2016.02.009.

[27] X.L. Wang, Y. Feng, V.R. Swail, A. Cox, Historical Changes in the Beaufort–Chukchi–Bering Seas Surface Winds and Waves, 1971–2013, J. Climate. 28 (2015) 7457–7469. https://doi.org/10.1175/JCLI-D-15-0190.1.

[28] IPCC, Climate Change 2013: The Physical Science Basis. Contribution of Working Group I to the Fifth Assessment Report of the Intergovernmental Panel on Climate Change, Cambridge University Press, Cambridge, United Kingdom and New York, NY, USA, 2018.

[29] S. Saha, S. Moorthi, H.-L. Pan, X. Wu, J. Wang, S. Nadiga, P. Tripp, R. Kistler, J. Woollen, D. Behringer, H. Liu, D. Stokes, R. Grumbine, G. Gayno, J. Wang, Y.-T. Hou, H. Chuang, H.-M.H. Juang, J. Sela, M. Iredell, R. Treadon, D. Kleist, P. Van Delst, D. Keyser, J. Derber, M. Ek, J. Meng, H. Wei, R. Yang, S. Lord, H. van den Dool, A. Kumar, W. Wang, C. Long, M. Chelliah, Y. Xue, B. Huang, J.-K. Schemm, W. Ebisuzaki, R. Lin, P. Xie, M. Chen, S. Zhou, W. Higgins, C.-Z. Zou, Q. Liu, Y. Chen, Y. Han, L. Cucurull, R.W. Reynolds, G. Rutledge, M. Goldberg, The NCEP Climate Forecast System Reanalysis, Bull. Amer. Meteor. Soc. 91 (2010) 1015–1058. https://doi.org/10.1175/2010BAMS3001.1.

[30] F.W. Poole, G.L. Hufford, Meteorological and oceanographic factors affecting sea ice in cook inlet, Journal of Geophysical Research: Oceans. 87 (1982) 2061–2070. https://doi.org/10.1029/JC087iC03p02061.

776 [31] N. Booij, R.C. Ris, L.H. Holthuijsen, A third-generation wave model for coastal regions
777 1. Model description and validation, J. Geophys. Res. 104 (1999) 7649–7666.
778 https://doi.org/10.1029/98JC02622.
779 [32] R.C. Ris, L.H. Holthuijsen, N. Booij, A third-generation wave model for coastal regions
780 2. Verification, J. Geophys. Res. 104 (1999) PP. 7667-7681.
781 https://doi.org/199910.1029/1998JC900123.
782 [33] G.J. Komen, K. Hasselmann, K. Hasselmann, On the Existence of a Fully Developed
783 Wind-Sea Spectrum, J. Phys. Oceanogr. 14 (1984) 1271–1285. https://doi.org/10.1175/1520-
784 0485(1984)014<1271:OTEOAF>2.0.CO;2.
785 [34] L. Cavaleri, P.M. Rizzoli, Wind wave prediction in shallow water: Theory and
786 applications, Journal of Geophysical Research: Oceans. 86 (1981) 10961–10973.
787 https://doi.org/10.1029/JC086iC11p10961.
788 [35] S. Hasselmann, K. Hasselmann, J.H. Allender, T.P. Barnett, Computations and
789 Parameterizations of the Nonlinear Energy Transfer in a Gravity-Wave Specturm. Part II:
790 Parameterizations of the Nonlinear Energy Transfer for Application in Wave Models,
791 Journal of Physical Oceanography. 15 (1985) 1378–1391. https://doi.org/10.1175/1520-
792 0485(1985)015<1378:CAPOTN>2.0.CO;2.
793 [36] K. Hasselmann, T.P. Barnett, E. Bouws, H. Carlson, D.E. Cartwright, K. Enke, J.A.
794 Ewing, H. Gienapp, D.E. Hasselmann, P. Kruseman, A. Meerburg, P. Mueller, D.J. Olbers,
795 K. Richter, W. Sell, H. Walden, Measurements of wind-wave growth and swell decay during
796 the Joint North Sea Wave Project (JONSWAP), Ergaenzungsheft Zur Deutschen
797 Hydrographischen Zeitschrift. A (1973) 95 pp.
798 [37] J.A. Battjes, J.P.F.M. Janssen, Energy loss and set-up due to breaking of random waves,
799 in: 16th International Conference on Coastal Engineering, ASCE, Hamburg, Germany, 1978:
800 pp. 569–587.
801 [38] N. Guillou, G. Lavidas, G. Chapalain, Wave Energy Resource Assessment for
802 Exploitation—A Review, Journal of Marine Science and Engineering. 8 (2020) 705.
803 https://doi.org/10.3390/jmse8090705.
804 [39] K.A. Haas, Assessment of Energy Production Potential from Ocean Currents along the
805 United States Coastline, (2013). https://doi.org/10.2172/1220255.
806 [40] M.R. Hashemi, M. Lewis, Wave-Tide Interactions in Ocean Renewable Energy, in: Z.
807 Yang, A. Copping (Eds.), Marine Renewable Energy: Resource Characterization and
808 Physical Effects, Springer International Publishing, Cham, 2017: pp. 137–158.
809 https://doi.org/10.1007/978-3-319-53536-4_6.
810 [41] M. Zijlema, Computation of wind-wave spectra in coastal waters with SWAN on
811 unstructured grids, Coastal Engineering. 57 (2010) 267–277.
812 https://doi.org/10.1016/j.coastaleng.2009.10.011.
813 [42] B.R.D. Robertson, C.E. Hiles, B.J. Buckham, Characterizing the near shore wave energy
814 resource on the west coast of Vancouver Island, Canada, Renewable Energy. 71 (2014) 665–
815 678. https://doi.org/10.1016/j.renene.2014.06.006.
816 [43] M.N. Allahdadi, B. Gunawan, J. Lai, R. He, V.S. Neary, Development and validation of a
817 regional-scale high-resolution unstructured model for wave energy resource characterization
818 along the US East Coast, Renewable Energy. 136 (2019) 500–511.
819 https://doi.org/10.1016/j.renene.2019.01.020.

[44] H. Karunarathna, P. Maduwantha, B. Kamranzad, H. Rathnasooriya, K. de Silva, Evaluation of spatio-temporal variability of ocean wave power resource around Sri Lanka, Energy. 200 (2020) 117503. https://doi.org/10.1016/j.energy.2020.117503.
[45] M. Bernardino, L. Rusu, C. Guedes Soares, Evaluation of the wave energy resources in the Cape Verde Islands, Renewable Energy. 101 (2017) 316–326. https://doi.org/10.1016/j.renene.2016.08.040.
[46] R.L.K. Lokuliyana, M. Folley, S.D.G.S.P. Gunawardane, P.N. Wickramanayake, Sri Lankan wave energy resource assessment and characterisation based on IEC standards, Renewable Energy. (2020). https://doi.org/10.1016/j.renene.2020.08.005.
[47] L. Rusu, The wave and wind power potential in the western Black Sea, Renewable Energy. 139 (2019) 1146–1158. https://doi.org/10.1016/j.renene.2019.03.017.
[48] C. Lo Re, G. Manno, G. Ciraolo, G. Besio, Wave Energy Assessment around the Aegadian Islands (Sicily), Energies. 12 (2019) 333. https://doi.org/10.3390/en12030333.
[49] M. Gonçalves, P. Martinho, C. Guedes Soares, Wave energy assessment based on a 33-year hindcast for the Canary Islands, Renewable Energy. 152 (2020) 259–269. https://doi.org/10.1016/j.renene.2020.01.011.
[50] Y. Lin, S. Dong, Z. Wang, C. Guedes Soares, Wave energy assessment in the China adjacent seas on the basis of a 20-year SWAN simulation with unstructured grids, Renewable Energy. 136 (2019) 275–295. https://doi.org/10.1016/j.renene.2019.01.011.
[51] X. Lastiri, S. Abadie, P. Maron, M. Delpey, P. Liria, J. Mader, V. Roeber, Wave Energy Assessment in the South Aquitaine Nearshore Zone from a 44-Year Hindcast, Journal of Marine Science and Engineering. 8 (2020) 199. https://doi.org/10.3390/jmse8030199.
[52] K. Amarouche, A. Akpınar, N.E.I. Bachari, F. Houma, Wave energy resource assessment along the Algerian coast based on 39-year wave hindcast, Renewable Energy. 153 (2020) 840–860. https://doi.org/10.1016/j.renene.2020.02.040.
[53] J. Morim, N. Cartwright, A. Etemad-Shahidi, D. Strauss, M. Hemer, Wave energy resource assessment along the Southeast coast of Australia on the basis of a 31-year hindcast, Applied Energy. 184 (2016) 276–297. https://doi.org/10.1016/j.apenergy.2016.09.064.
[54] W.-C. Wu, Z. Yang, T. Wang, Wave Resource Characterization Using an Unstructured Grid Modeling Approach, Energies. 11 (2018) 605. https://doi.org/10.3390/en11030605.
[55] N. Guillou, G. Chapalain, Numerical modelling of nearshore wave energy resource in the Sea of Iroise, Renewable Energy. 83 (2015) 942–953. https://doi.org/10.1016/j.renene.2015.05.021.
[56] E. Lim, B.W. Eakins, R. Wigley, Coastal Relief Model of Southern Alaska: Procedures, Data Sources, and Analysis, NOAA Technical Memorandum NESDIS NGDC-43, 2011.
[57] M. Zimmermann, M.M. Prescott, Smooth Sheet Bathymetry of Cook Inlet, Alaska, NOAA Technical Memorandum NMFS-AFSC-275, 2014.
[58] M. Zimmermann, M.M. Prescott, Smooth Sheet Bathymetry of the Central Gulf of Alaska, NOAA Technical Memorandum NMFS-AFSC-287, 2015. 10.7289/V5GT5K4F.
[59] M. Zimmermann, M.M. Prescott, Smooth Sheet Bathymetry of the Aleutian Islands, NOAA Technical Memorandum NMFS-AFSC-250, 2013.
[60] Z. Yang, W.-C. Wu, T. Wang, G. Garcia Medina, L. Castrucci, High-Resolution Regional Wave Hindcast for the U.S. Alaska Coast, (2019). https://doi.org/10.2172/1579259.
[61] A. Chawla, D.M. Spindler, H.L. Tolman, Validation of a thirty year wave hindcast using the Climate Forecast System Reanalysis winds, Ocean Modelling. 70 (2013) 189–206. https://doi.org/10.1016/j.ocemod.2012.07.005.

[62] F. Ardhuin, E. Rogers, A.V. Babanin, J.-F. Filipot, R. Magne, A. Roland, A. van der Westhuysen, P. Queffeulou, J.-M. Lefevre, L. Aouf, F. Collard, Semiempirical Dissipation Source Functions for Ocean Waves. Part I: Definition, Calibration, and Validation, J. Phys. Oceanogr. 40 (2010) 1917–1941. https://doi.org/10.1175/2010JPO4324.1.
[63] H.L. Tolman, Treatment of unresolved islands and ice in wind wave models, Ocean Modelling. 5 (2003) 219–231. https://doi.org/10.1016/S1463-5003(02)00040-9.
[64] P. Doubrawa Moreira, G.N. Scott, W.D. Musial, L.F. Kilcher, C. Draxl, E.J. Lantz, Offshore Wind Energy Resource Assessment for Alaska, (2018). https://doi.org/10.2172/1417728.
[65] J. Sierra, M. Casas-Prat, E. Campins, Impact of climate change on wave energy resource: The case of Menorca (Spain), Renewable Energy. 101 (2017) 275–285.
[66] M. Gonçalves, P. Martinho, C.G. Soares, A 33-year hindcast on wave energy assessment in the western French coast, Energy. 165 (2018) 790–801.
[67] B. Kamranzad, A. Etemad-Shahidi, V. Chegini, Developing an optimum hotspot identifier for wave energy extracting in the northern Persian Gulf, Renewable Energy. 114 (2017) 59–71.
[68] R.P. Patel, G. Nagababu, S.V.V. Arun Kumar, S. M., S.S. Kachhwaha, Wave resource assessment and wave energy exploitation along the Indian coast, Ocean Engineering. 217 (2020) 107834. https://doi.org/10.1016/j.oceaneng.2020.107834.
[69] M.A. Hemer, S. Zieger, T. Durrant, J. O'Grady, R.K. Hoeke, K.L. McInnes, U. Rosebrock, A revised assessment of Australia's national wave energy resource, Renewable Energy. 114 (2017) 85–107. https://doi.org/10.1016/j.renene.2016.08.039.
[70] Z. Yang, G. García-Medina, W.-C. Wu, T. Wang, L.R. Leung, L. Castrucci, G. Mauger, Modeling analysis of the swell and wind-sea climate in the Salish Sea, Estuarine, Coastal and Shelf Science. 224 (2019) 289–300. https://doi.org/10.1016/j.ecss.2019.04.043.
[71] K. Christakos, B.R. Furevik, O.J. Aarnes, Ø. Breivik, L. Tuomi, Ø. Byrkjedal, The importance of wind forcing in fjord wave modelling, Ocean Dynamics. 70 (2020) 57–75. https://doi.org/10.1007/s10236-019-01323-w.
[72] D. Anderson, P. Ruggiero, J.A.A. Antolínez, F.J. Méndez, J. Allan, A Climate Index Optimized for Longshore Sediment Transport Reveals Interannual and Multidecadal Littoral Cell Rotations, Journal of Geophysical Research: Earth Surface. 123 (2018) 1958–1981. https://doi.org/10.1029/2018JF004689.
[73] K.M. Bailey, S.A. Macklin, R.K. Reed, R.D. Brodeur, W.J. Ingraham, J.F. Piatt, M. Shima, R.C. Francis, P.J. Anderson, T.C. Royer, A. Hollowed, D.A. Somerton, W.S. Wooster, ENSO events in the northern Gulf of Alaska, and effects on selected marine fisheries, 1995. http://pubs.er.usgs.gov/publication/2002017.
[74] A. Melsom, E.J. Metzger, H.E. Hurlburt, Impact of remote oceanic forcing on Gulf of Alaska sea levels and mesoscale circulation, Journal of Geophysical Research: Oceans. 108 (2003). https://doi.org/10.1029/2002JC001742.
[75] H.J. Niebauer, R.H. Day, Causes of interannual variability in the sea ice cover of the Eastern Bering Sea, GeoJournal. 18 (1989) 45–59. https://doi.org/10.1007/BF00722385.
[76] B.G. Reguero, I.J. Losada, F.J. Méndez, A global wave power resource and its seasonal, interannual and long-term variability, Applied Energy. 148 (2015) 366–380. https://doi.org/10.1016/j.apenergy.2015.03.114.

[77] N. Guillou, G. Chapalain, Annual and seasonal variabilities in the performances of wave energy converters, Energy. 165 (2018) 812–823. https://doi.org/10.1016/j.energy.2018.10.001.
[78] J.L. Hanson, B.A. Tracy, H.L. Tolman, R.D. Scott, Pacific Hindcast Performance of Three Numerical Wave Models, J. Atmos. Oceanic Technol. 26 (2009) 1614–1633. https://doi.org/10.1175/2009JTECHO650.1.
[79] J. Bowers, I. Morton, G. Mould, Directional statistics of the wind and waves, Applied Ocean Research. 22 (2000) 13–30.

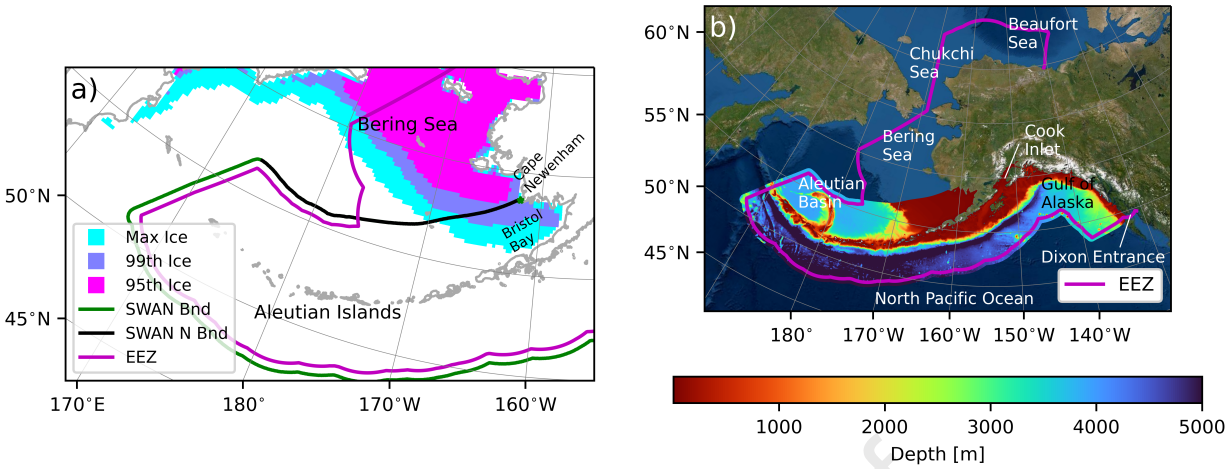

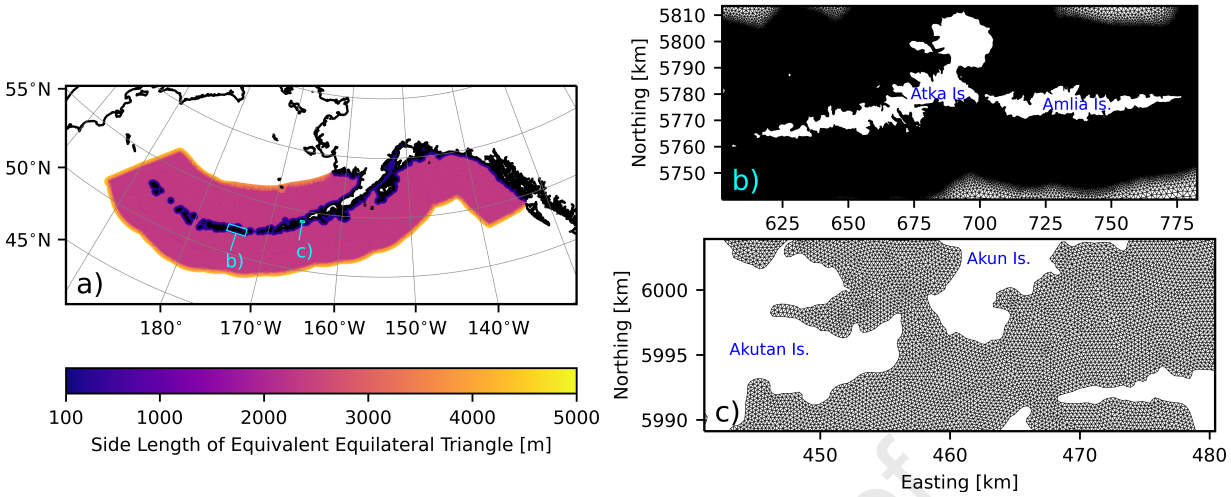

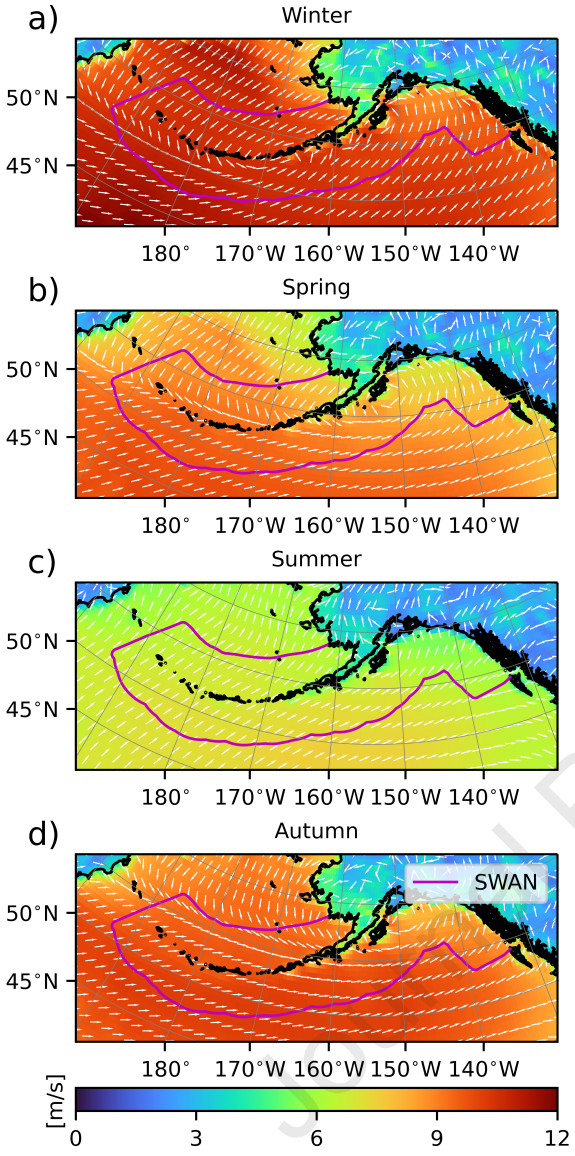

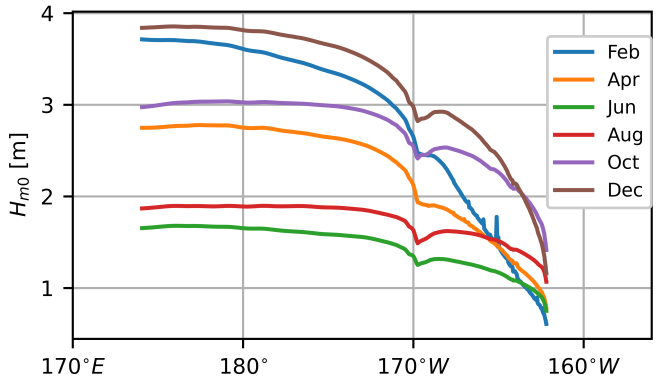

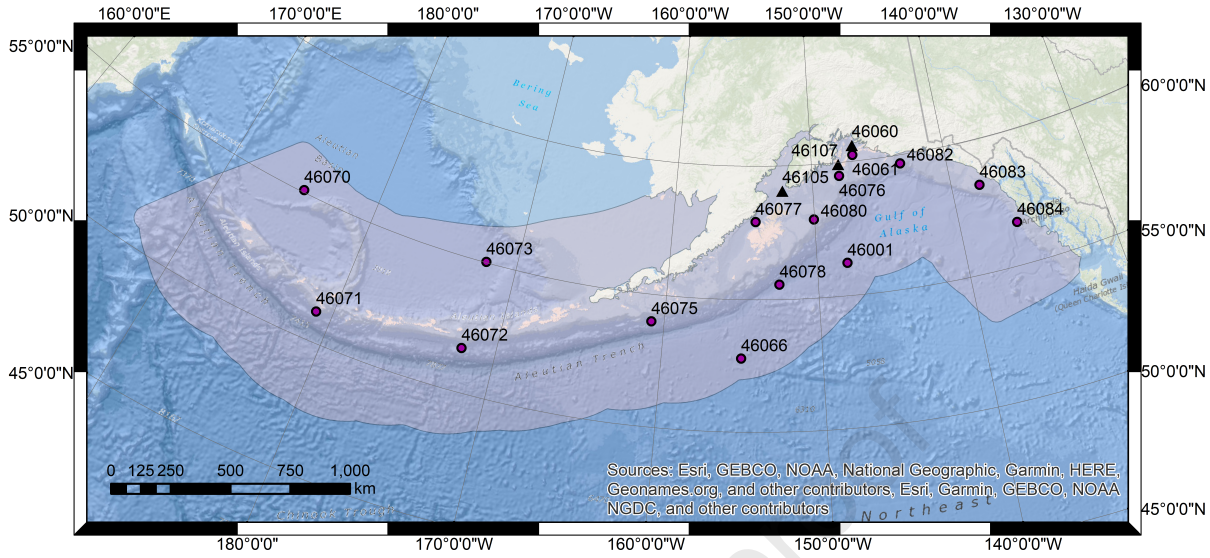

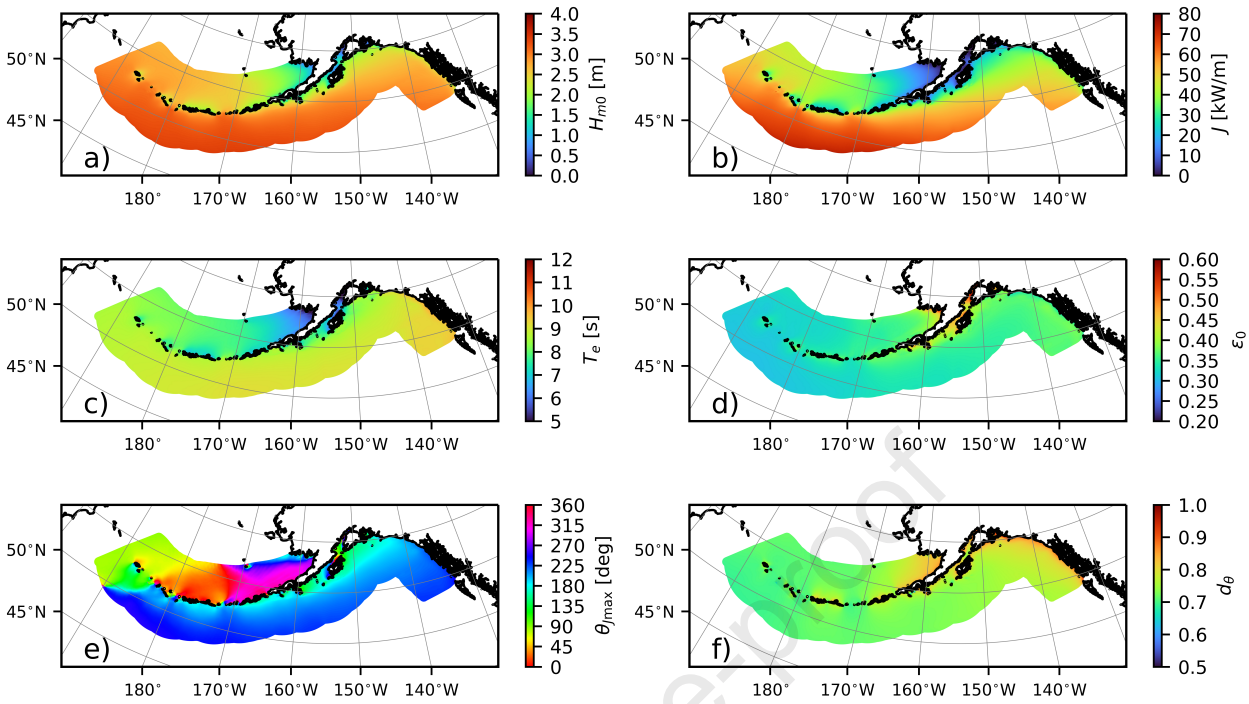

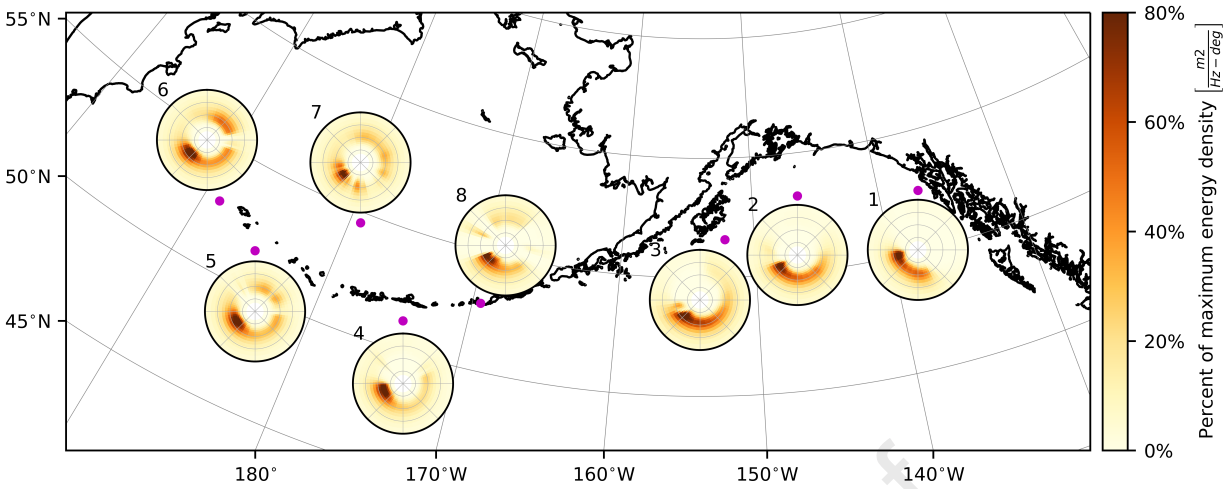

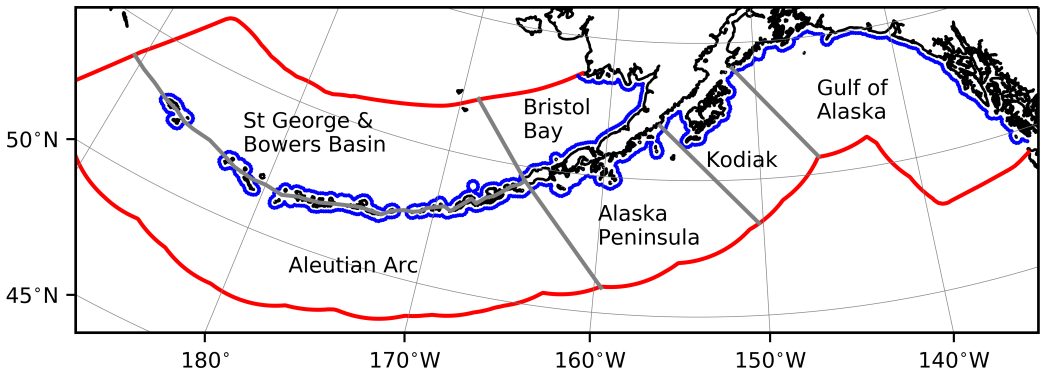

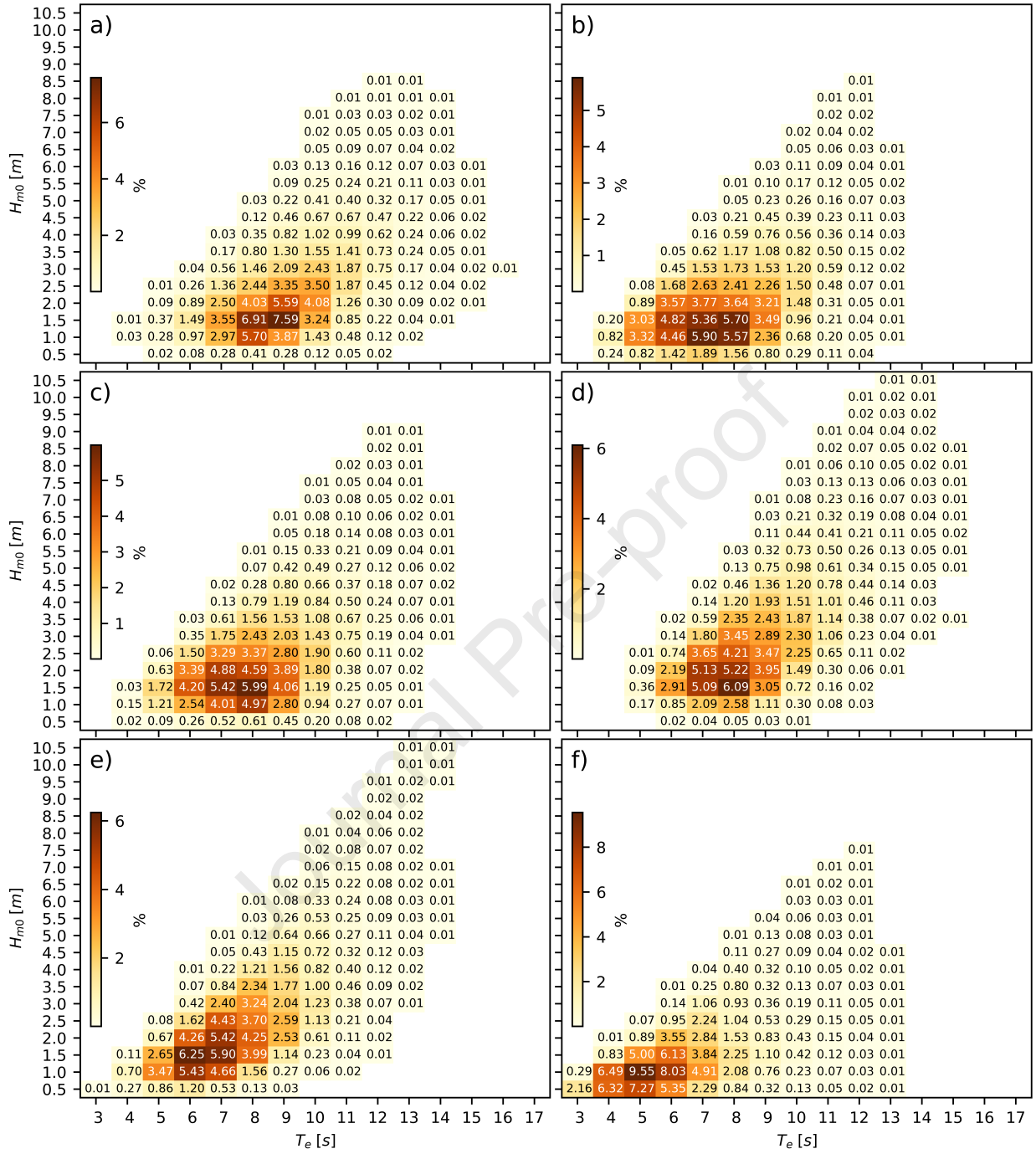

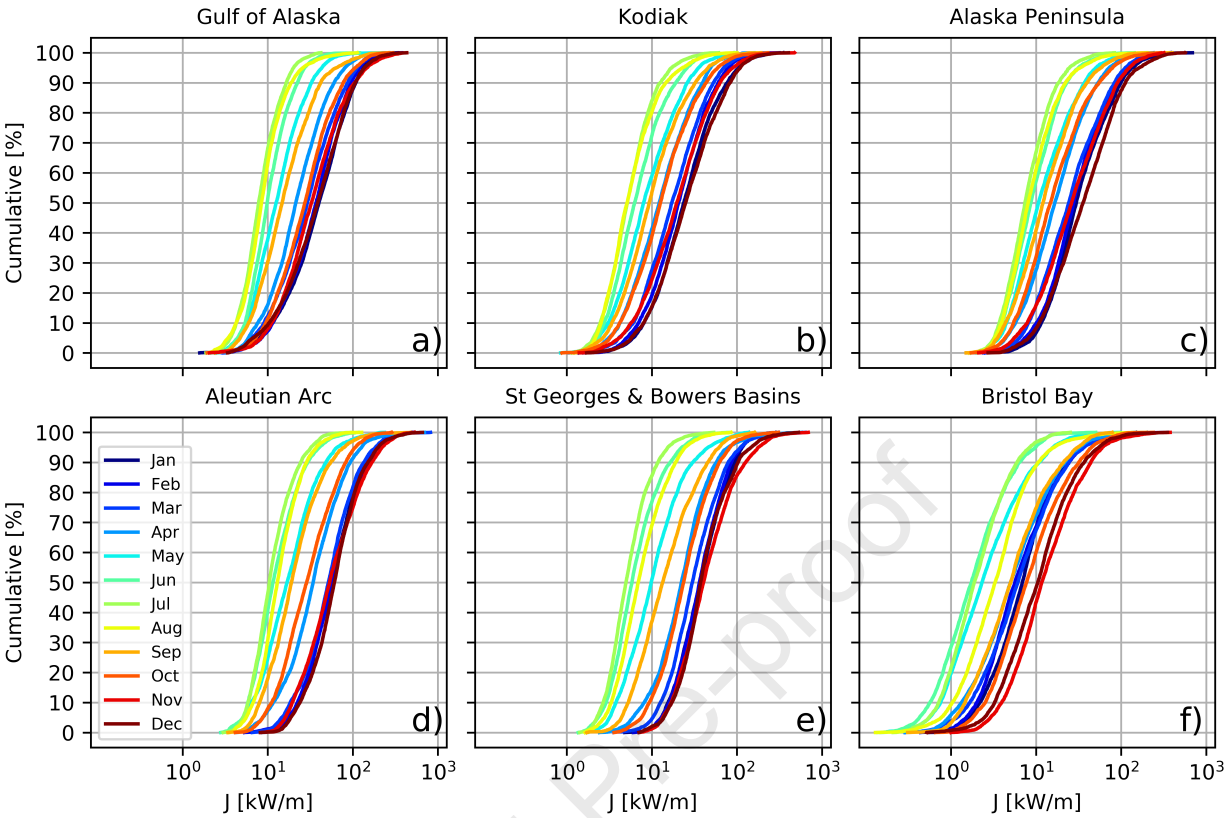

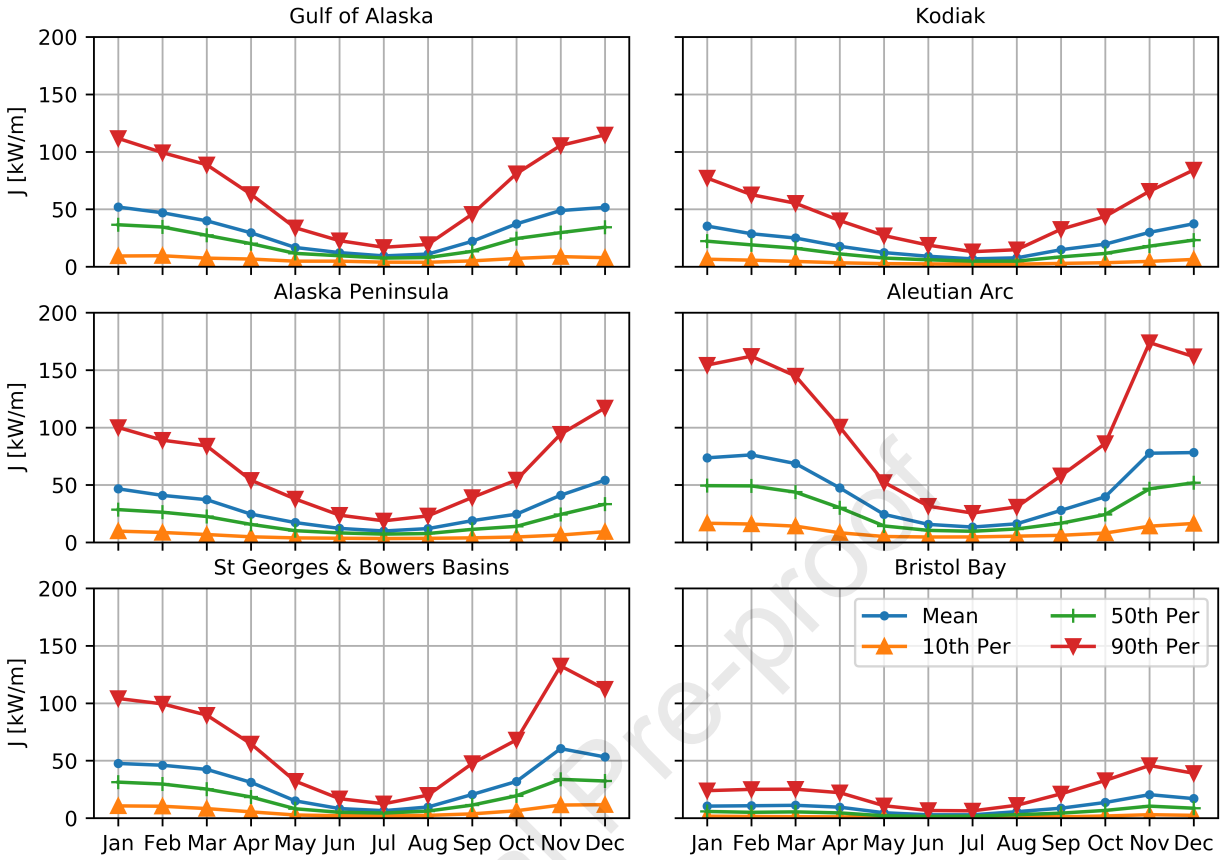

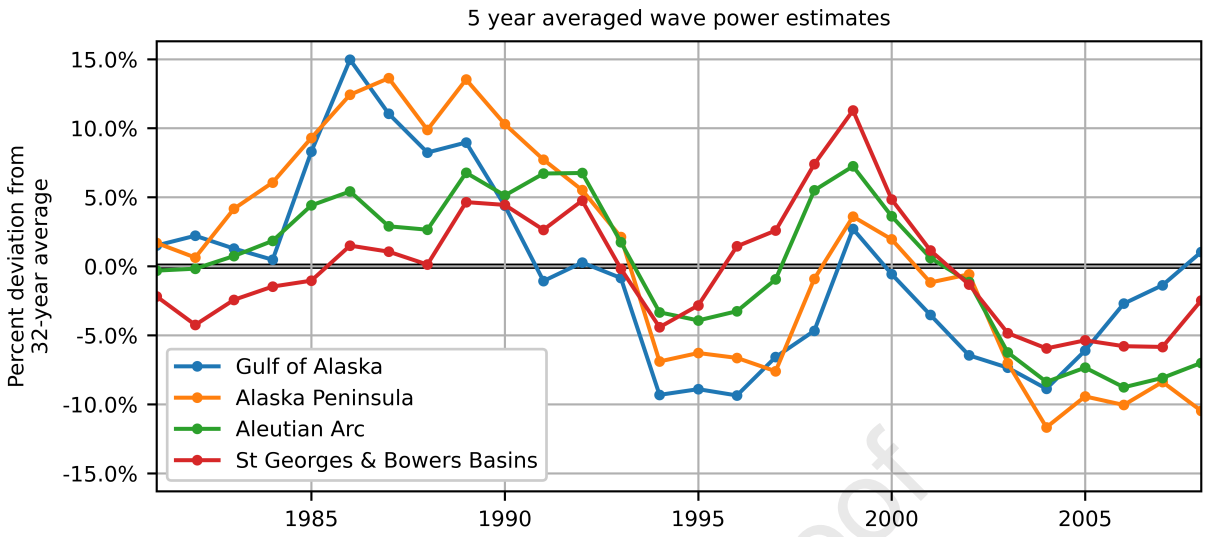

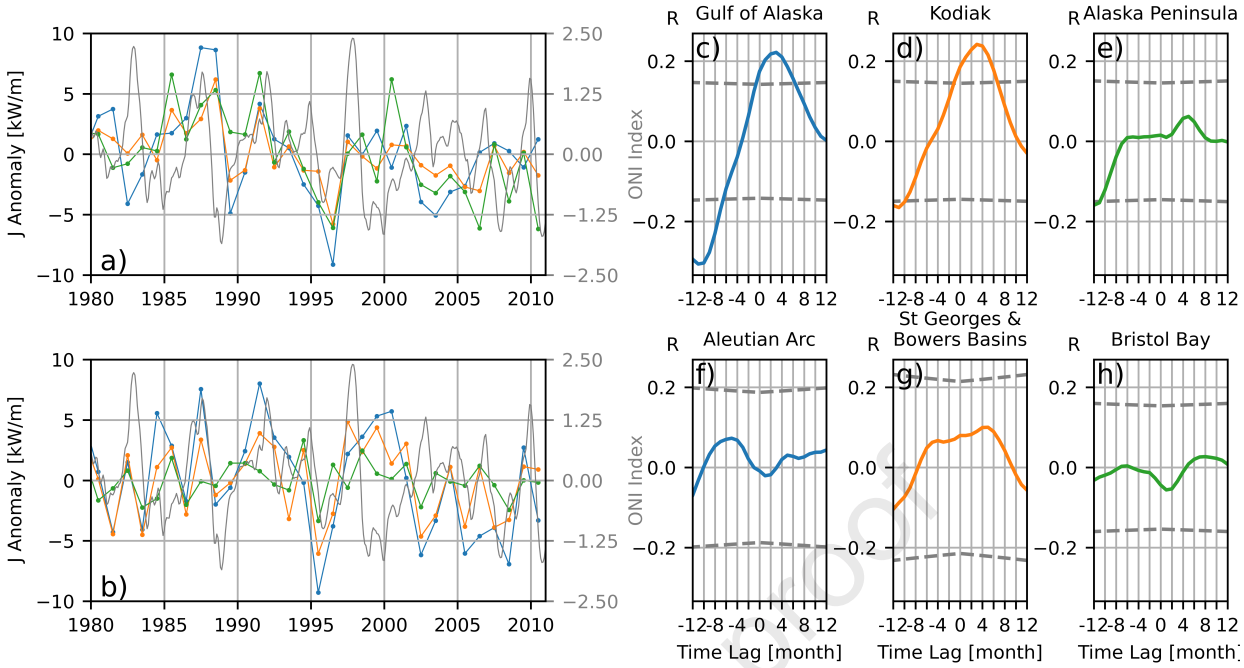

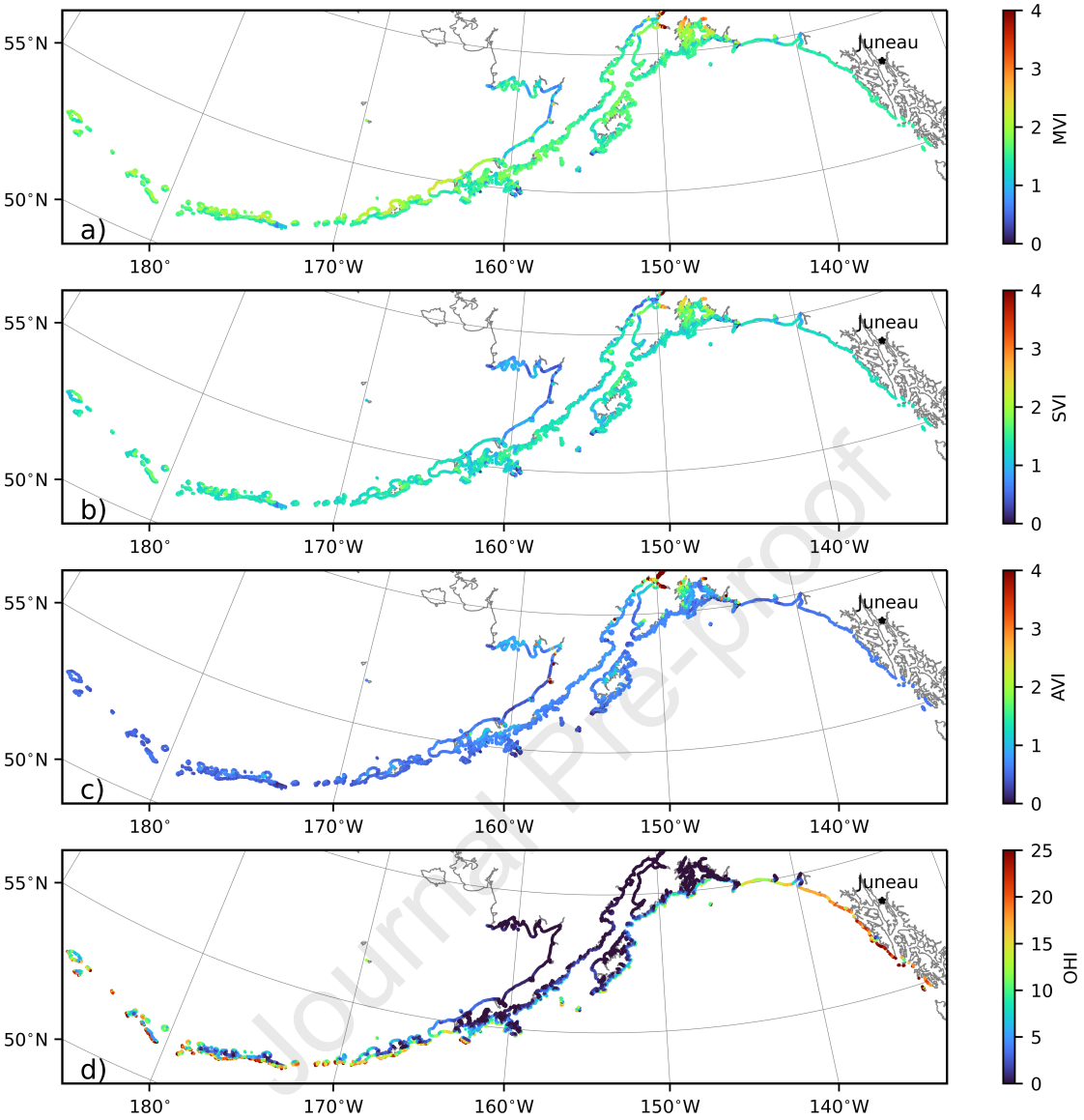

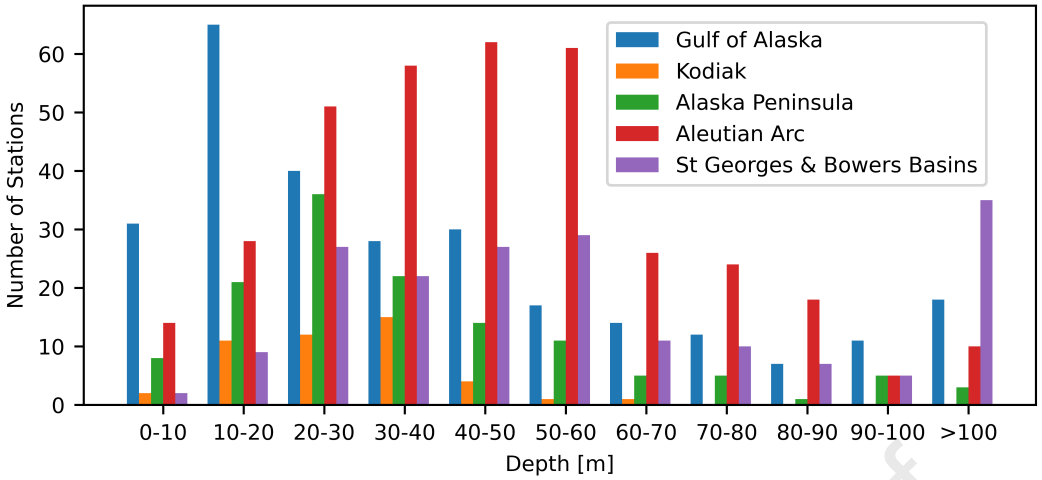

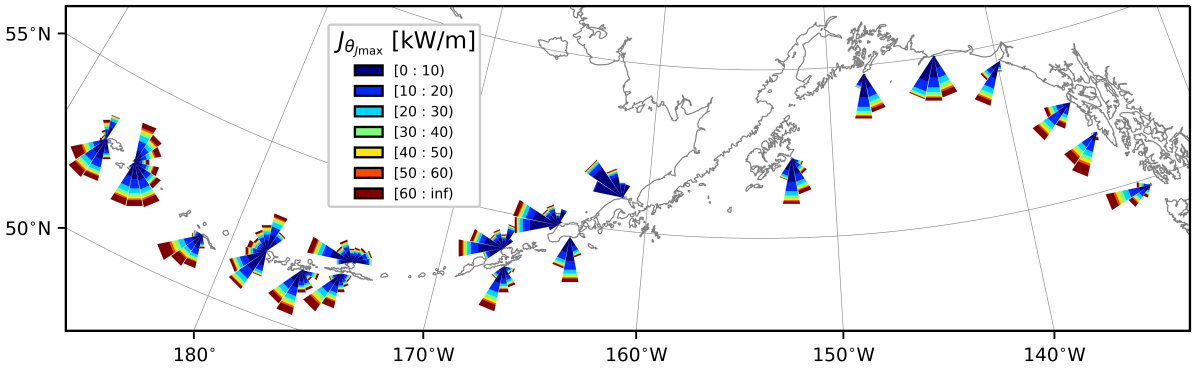

Highlights:

- A high-resolution wave model covering the southern Alaska coast was developed and validated.
- The first systemic wave resource characterization of southern Alaska following IEC-TS 62600-101
- The southern coast of the Aleutian Archipelago has the highest annual wave power at 45.4 kW/m
- Southeast Alaska and the Aleutian Archipelago had the most nearshore hotspots with Optimum Hotspot Identifier > 5 kW/m

Key words: wave energy resource, wave climate, Alaska Coast, SWAN, WW3

Declaration of interests

☒ The authors declare that they have no known competing financial interests or personal relationships that could have appeared to influence the work reported in this paper.

☐The authors declare the following financial interests/personal relationships which may be considered as potential competing interests: